# A NUMERICAL ANALYSIS OF RESTRAINED SHRINKAGE STRESSES IN ABLATION HEAT SHIELDS

---

A Thesis

Presented to

the Faculty of the School of Engineering and Applied Science

University of Virginia


In Partial Fulfillment

of the Requirements for the Degree

Master of Applied Mechanics

by

Marvin B. Dow

June 1969

APPROVAL SHEET

This thesis is submitted in partial fulfillment of

the requirements for the degree of

Master of Applied Mechanics

Marvin B. Now

Author

Approved:

Faculty Advisor

Dean, School of Engineering
and Applied Science

June 1969

TABLE OF CONTENTS

## ABSTRACT

An approximate method is presented for analyzing restrained shrinkage stresses in ablation heat shields during space flight cooling. An alternating direction iterative method is used to obtain numerical solutions of a two-dimensional mixed boundary-value problem for rectangular elastic plates. Plane strain theory is assumed with the heat-shield length and thicknesses as controlling dimensions and the finite difference method is used to integrate the governing differential equations for displacements and stresses. The calculated stresses are shown to agree with exact results well away from the heat-shield edges. At the restrained-free edge corner of the heat shield, the calculated stresses do not agree with the prescribed boundary stresses. It is concluded that calculated stresses are valid for regions other than the corner vicinity, but are not valid near the corner.

Experimental results from cold soak tests of ablation heat-shield models are presented. These tests indicate that the location of maximum restrained shrinkage stress depends on the ablation material thickness. Calculated stresses are qualitatively compared with the test data. The calculations and the test data both indicate that heat shields constructed with unreinforced ablation materials are susceptible to edge cracking when the ablation material thickness exceeds about 0.5 inch.

ACKNOWLEDGMENTS

The author is indebted to the National Aeronautics and Space Administration for permission to use material from research at the Langley Research Center in this thesis. Gratitude is expressed to Mr. Louis F. Vosteen and William A. Brooks, Jr., his supervisors in the Entry Structures Branch, Structures Research Division, for their support of this work. Particular thanks are due Mrs. Kay L. Brinkley for programing the equations used in this thesis.

The author is also grateful to Professor Richard L. Jennings for his comments and suggestions during the preparation of this thesis.

LIST OF FIGURES

FIGURE PAGE

## LIST OF SYMBOLS

| | |
|---|---|
| A, B, C, D | elastic constants defined in Table I of Appendix A |
| b | plate length, in. |
| E | modulus of elasticity, lb/sq. in. |
| G | shear modulus, lb/sq. in. |
| h | plate thickness, in. |
| I | total number of mesh points in x-direction |
| J | total number of mesh points in z-direction |
| T | temperature, $^{o}F$ |
| $\Delta T$ | temperature change from reference temperature, $^{o}F$ |
| u | displacement in x-direction, in. |
| v | displacement in y-direction, in. |
| w | displacement in z-direction, in. |
| x, y, z | rectangular Cartesian coordinates |
| $\Delta x$ | mesh spacing in the x-direction, in. |
| $\Delta z$ | mesh spacing in the z-direction, in. |
| $\alpha$ | coefficient of thermal expansion, in/in/$^{o}F$ |
| $\epsilon_y$ | substructure strain in y-direction, in/in. |
| $\lambda$ | Lame coefficient, lb/sq. in. |
| $\nu$ | Poisson's ratio |
| $\sigma$ | normal stress, lb/sq. in. |
| $\tau$ | shear stress, lb/sq. in. |

Subscripts

| | |
|---|---|
| m,n | integers |
| s | indicates substructure material properties and temperature |
| x,y,z | indicates direction of normal and shear stresses and also partial differentiation |

# CHAPTER I

# INTRODUCTION

## 1.1 Research Problem

The effects of restrained shrinkage due to space flight cooling must be investigated prior to the materials selection and design of ablation heat shields for proposed multimission manned spacecraft. The multimission spacecraft concept involves a single vehicle structure which can be adapted for several space missions. The adaptation required for these spacecraft is a refurbishable heat-shielding system which will consist of ablation material panels with provision for removing and replacing the entire system. This thesis presents an approximate thermal-stress analysis method which is applicable to refurbishable heat shields. The method of analysis, programed for solution with a digital computer, provides a means to investigate how restrained shrinkage stresses in ablation materials are affected by temperature distribution, ablator strength properties, and ablator thickness.

Studies of refurbishable heat shields (Ref. 1) usually consider rectangular planform panels of ablation material bonded to substructure panels constructed of conventional materials such as steel or fiberglass. Figure 1 shows the arrangement of such panels on a conceptual spacecraft and Figure 2 shows some details of an individual panel. The ablation materials considered for these panels are specialized low-density-plastic composites which have low ultimate tensile

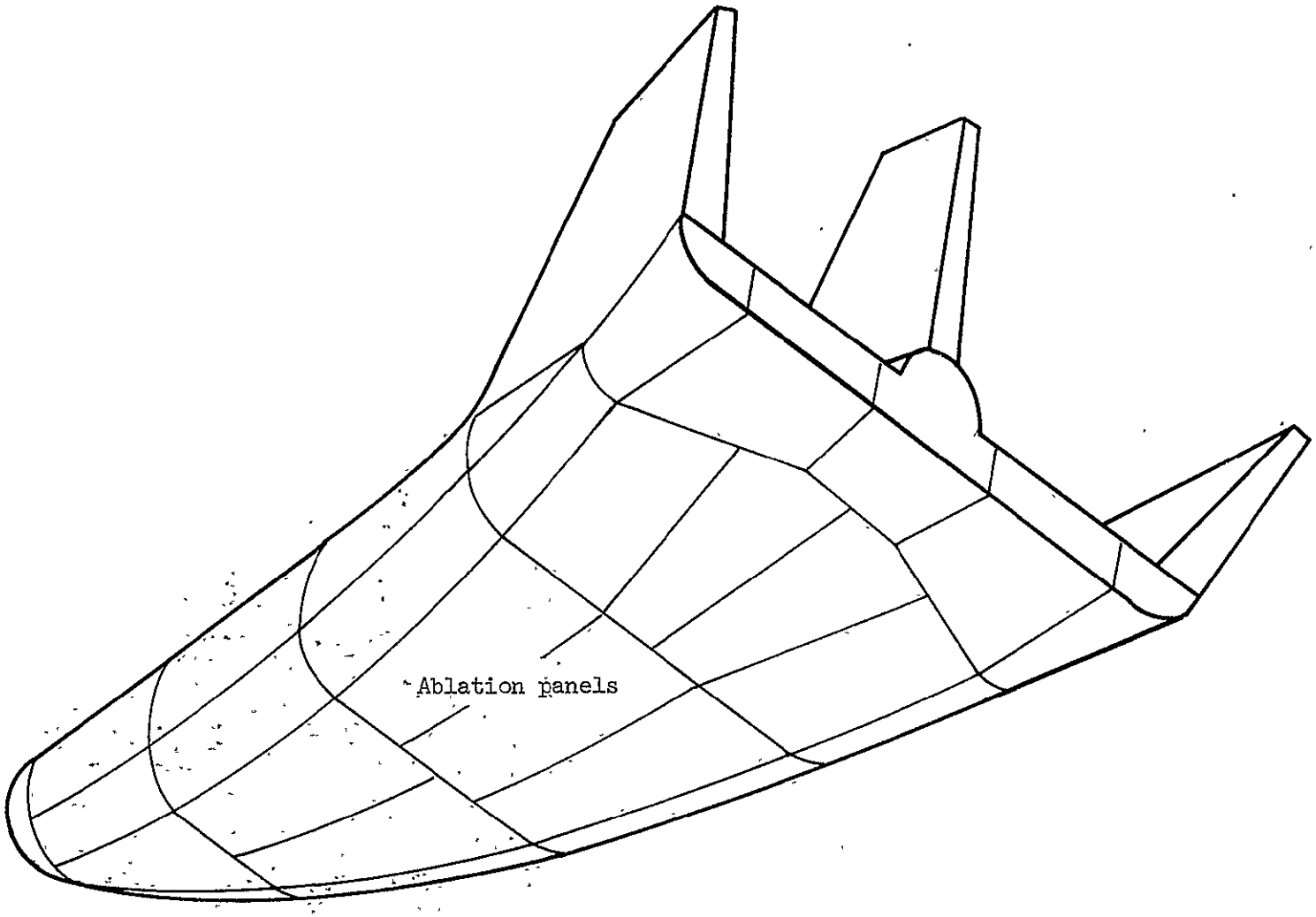


Figure 1.– Conceptual manned spacecraft with ablation heat-shield panels

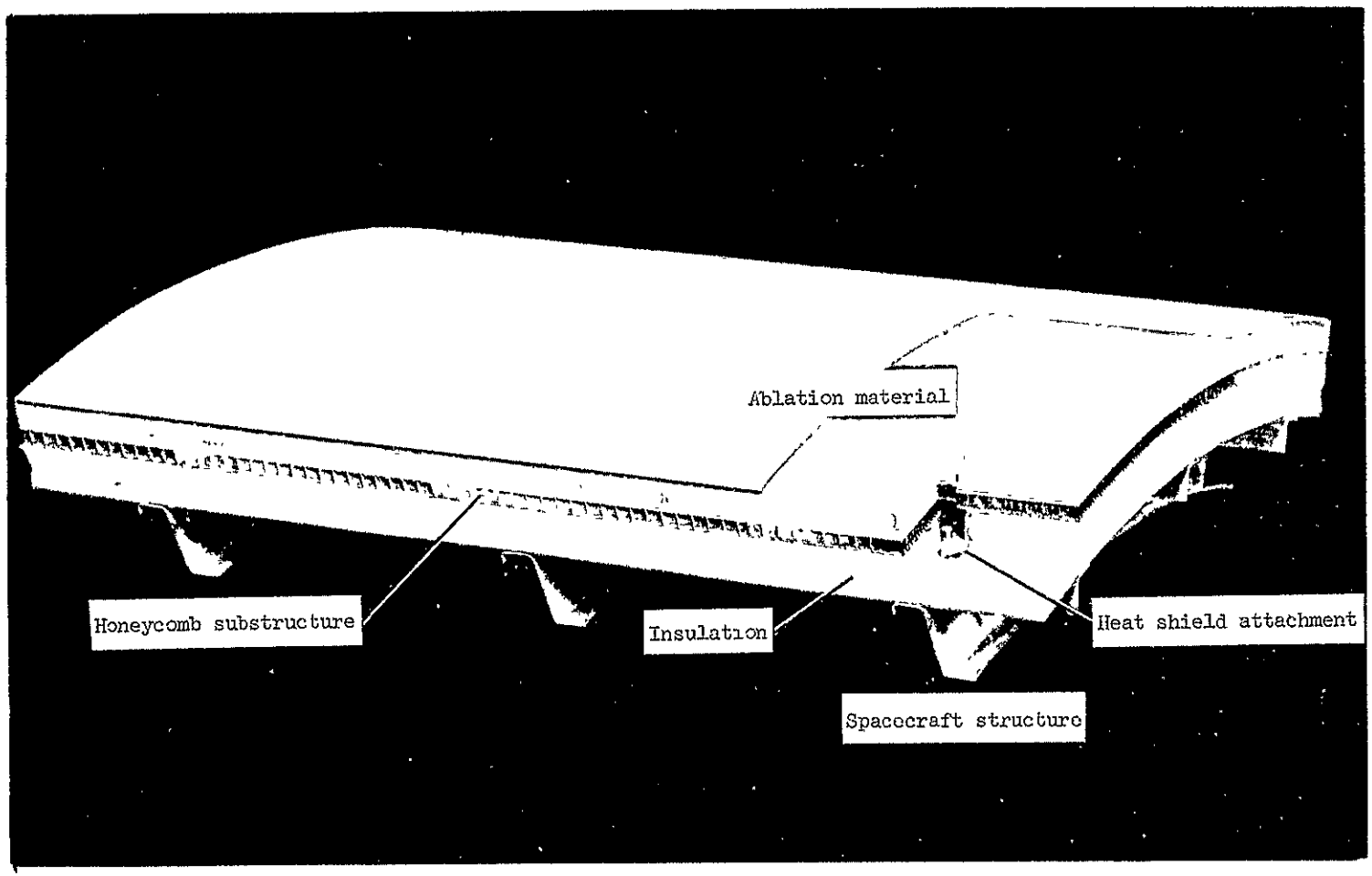


Figure 2.- Model of ablation heat-shield panel

strengths and high expansion coefficients. Since the heat-shield panels on the multimission vehicle will be continuously exposed to the space environment, the panels can experience severe cooling due to radiation heat transfer. This cooling will produce tension stresses in the ablation material because of differential thermal contraction between the ablation material and the substrate. The combination of tension stress and low ultimate strength can cause the ablation material to crack. From a design standpoint, cracks in the ablation material prior to reentry are unacceptable because the cracks compromise the structural integrity of the heat shield. Therefore, a technique for predicting restrained shrinkage stresses must be used during heat-shield design. Experiments conducted during this thesis investigation indicate that the location of maximum shrinkage stress varies with thickness and can be greatest at the edges of the heat shield. These data indicate the inadequacy of simplified shrinkage analyses which neglect edge effects.

In this thesis, the heat shield is approximated as a flat rectangular slab of ablation material bonded on one side to a stiff substructure. Plane strain theory is used with the heat-shield length and thickness as the controlling dimensions. The finite difference method is used to integrate the governing differential equations for displacements and stresses. Temperature gradients through the ablation material thickness and variations of elastic constants with temperature are permitted in the analysis. Thermal-stress calculations are compared with exact solutions and are qualitatively compared with

experimental data obtained during this investigation. The restrained shrinkage analysis involves solving a mixed boundary problem in that the bonded surface of the ablation material has prescribed displacements while all other surfaces have prescribed boundary stresses. Experimental and analytical studies of restrained shrinkage or expansion have been made by other persons. Some of these studies are discussed in the following section. With but one exception, the analytical methods used in these studies differ from the thesis method.

## 1.2 Historical Background of Research Problem

Thermal stresses in a rectangular plate, clamped along one edge, are analyzed in Reference 2. In this reference, plane stress theory is used and the thermal-stress problem with a uniform temperature change is converted to a problem of specified fictitious edge stresses. The integral representing the strain energy is expressed in terms of normal and shear stresses and minimized using the calculus of variations. The analytical results show a normal stress concentration factor of 10 at the corner junction of the free and clamped edges. The specified interface displacements are, however, not satisfied in this analysis.

The analyses of a rectangular plate with a clamped edge reported in References 3 and 4 assume plane stress theory and uniform temperature. In these analyses, the shear and normal stresses at the clamped edge are expressed in terms of Fourier series satisfying the differential equations of equilibrium. Numerical results given in both references show infinite normal and shear stresses at the clamped-free

edge corner. Reference 4 also presents calculated stresses for plate regions other than the clamped edge. The author states that these calculated stresses are valid since the corner stress singularity is local and confined to the corner vicinity.

Photoelastic studies of restrained shrinkage are reported in References 5, 6, and 7. The problems associated with bonding solid rocket propellant grains to rocket motor cases are the bases for these studies. The experimental data indicate stress concentrations at the clamped-free edge corners. In Reference 5, the author states that photoelastic measurements up to 0.001 inch from the corner showed rapidly increasing normal tension stresses with approach to the corner. The author discusses, but does not reconcile the discrepancy between his data and the requirements for compression normal stresses to satisfy the boundary conditions for plane strain.

The analysis of Reference 8 is a plane stress analysis of a rectangular plate clamped along one edge and subjected to a uniform temperature change. The mixed boundary-value problem is solved for the two-dimensional displacement equations of equilibrium using a finite difference method. The numerical results show large, but finite values for normal and shear stresses at the clamped-free edge corner. The author states that the results for other plate locations agree qualitatively with the results of Reference 4 and that the precise behavior of the solution at the corner is not known.

# CHAPTER II

# ANALYTICAL MODEL

An analytical model was established to calculate the restrained shrinkage stresses in a flat rectangular slab of ablation material bonded to a substructure. Figure 3 shows the model configuration and identifies the rectangular Cartesian coordinate directions. The substructure of an actual heat shield would consist of structural elements such as honeycomb sandwich (see Fig. 2) or face sheets and stringers, but for this analysis the substructure is simply a restraining foundation for the ablation material.

## 2.1 Assumptions

The assumptions used in the analysis are discussed in the following paragraphs.

As shown in Figure 3, the x-y plane is the bonded interface between the ablation material and the substructure. The analysis is applied to the x-z plane, indicated by the heavy dashed line in Figure 3, whose bounded edge coincides with the line $-b \leq x \leq +b$, $z = 0$. The two-dimensional displacement vector of the plane has the components $u(x,z)$ in the x-direction and $w(x,z)$ in the z-direction. The two-dimensional approximation simplifies the analysis, and it is reasonable from consideration of the heat-shield dimensions. The typical $x$ and $y$ dimensions for the ablation material on an actual heat shield would

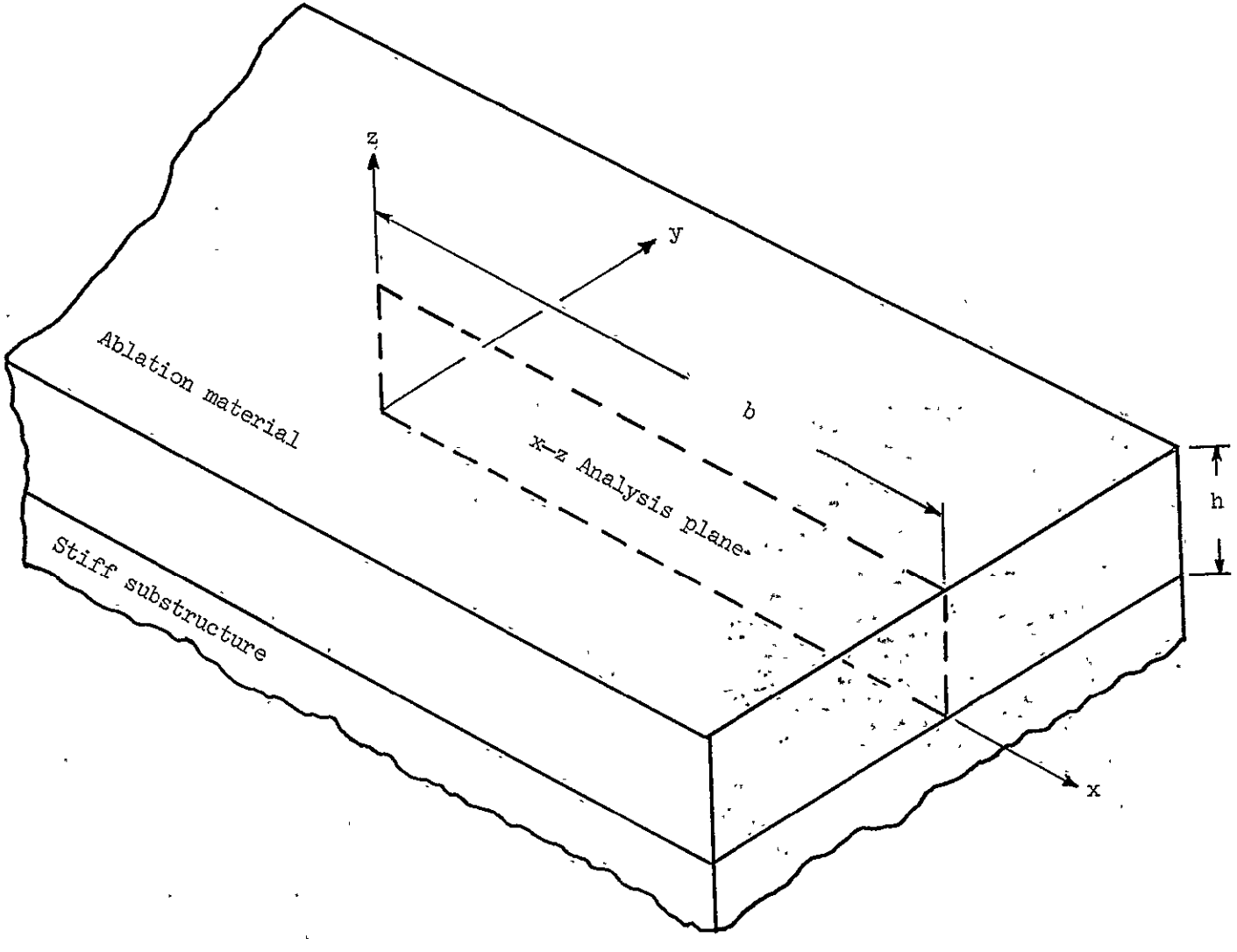


Figure 3.– Analysis model configuration and coordinate system

be between one and two orders of magnitude greater than the thickness. Therefore, if the heat-shield corner regions are excluded, a large area remains for which a two-dimensional approximation is applicable.

It is assumed that the ablation material is fixed to the substructure at $z = 0$ with a bonding material having negligible thickness and that the composite panel is free to expand or contract, but restrained against curvature. Displacements at the bonded interface ($z = 0$) are determined from the substructure temperature change and coefficient of thermal expansion only. This assumption is based on the material property data for typical ablation materials which are reported in References 9 and 10. These data indicate that the ablation materials have Young's moduli which are much smaller than those of conventional structural materials such as steel or aluminum. Therefore, the substructure is much stiffer than the ablation material and stresses in the ablation material will not produce significant substructure displacements. The exterior surfaces of the ablation material are assumed free of external loads. This assumption is realistic because the aerodynamic forces on the heat-shield surface are negligible during space flight.

The analysis assumes that temperature variations occur only through the thickness of the ablation material, the z-direction. This assumption is also reasonable because heat-shield cooling results from radiation to deep space from the exterior x-y surface of the ablation

material (see Fig. 3) and the cooling rate will be uniform over this surface.

The ablation materials considered in this analysis are uniform density mixtures without honeycomb reinforcement. These materials are assumed to be isotropic and elastic with the properties $E$ and $\alpha$ being functions of temperature only. Except for the initial cooling period, the ablation material temperature distribution will be fairly independent of time. Therefore, a steady-state temperature distribution is assumed. Heat-transfer analyses for calculating the temperature distribution are available (Ref. 11, for example).

For this analysis, it is assumed that the deformations of the x-z plane, which is located well away from the heat-shield corners, are described by plane strain theory. The ablation material strain in the y-direction ($\epsilon_y$) is assumed to be equal to the substructure strain. Since the substructure is assumed free to expand or contract, the value for $\epsilon_y$ is equal to $\alpha_s \Delta T_s$.

## 2.2 Governing Equations

Figure 4 shows the mixed boundary conditions on the x-z plane which are analyzed for $u$ and $w$ displacements. The bonded edge of the ablation material $-b \leq x \leq +b$, $z = 0$ has prescribed displacements while the other boundaries have prescribed stresses. Since the temperature and material properties are constant in the x-direction

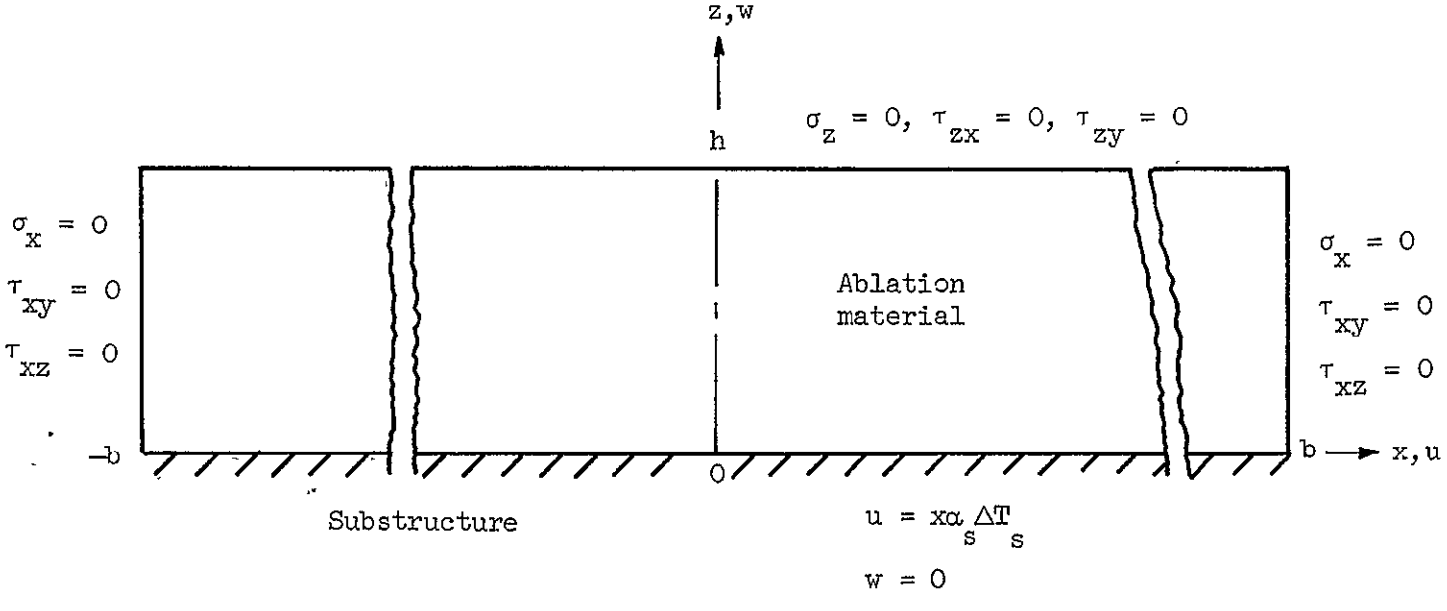


Figure 4.– Analysis plane showing assumed boundary conditions

and boundary conditions on the x-faces are identical, the z-axis is a line of symmetry. These symmetry conditions are

$$u = u_z = 0 \quad \text{on} \quad x = 0, \quad 0 \leq z \leq h \tag{1}$$

Therefore only the rectangle $0 \leq x \leq b$, $0 \leq z \leq h$ is considered. The analysis is formulated in terms of displacements rather than stress functions because displacement boundary conditions can be prescribed on the x-axis, but stresses on this axis can only be determined from the thermal-stress solution.

From Reference 12, the two-dimensional stress equilibrium equations are

$$\begin{aligned} \frac{\partial}{\partial x}(\sigma_x) + \frac{\partial}{\partial z}(\tau_{xz}) &= 0 \\ \frac{\partial}{\partial z}(\sigma_z) + \frac{\partial}{\partial x}(\tau_{zx}) &= 0 \end{aligned} \tag{2}$$

The thermoelastic relations between stress and strain are (Ref. 12)

$$\begin{aligned} \sigma_x &= \lambda e + 2G\epsilon_x - \frac{\alpha E \, \Delta T}{1 - 2\nu} \\ \sigma_y &= \lambda e + 2G\epsilon_y - \frac{\alpha E \, \Delta T}{1 - 2\nu} \\ \sigma_z &= \lambda e + 2G\epsilon_z - \frac{\alpha E \, \Delta T}{1 - 2\nu} \end{aligned} \tag{3}$$

$$\tau_{xy} = G\gamma_{xy}, \quad \tau_{yz} = G\gamma_{yz}, \quad \tau_{xz} = G\gamma_{xz}$$

where

$$\lambda = \frac{\nu E}{(1 + \nu)(1 - 2\nu)}, \quad G = \frac{E}{2(1 + \nu)} \quad \text{and} \quad e = \epsilon_x + \epsilon_y + \epsilon_z$$

Assuming linear strain displacement relationships, that is,

$$\epsilon_x = \frac{\partial u}{\partial x}, \quad \epsilon_z = \frac{\partial w}{\partial z}, \quad \gamma_{xz} = \left(\frac{\partial u}{\partial z} + \frac{\partial w}{\partial x}\right) \ldots$$

and substituting equations (3) into equations (2), the two-dimensional equilibrium equations for plane strain in terms of displacements may be written as

$$\begin{aligned}
&\frac{\partial}{\partial x}\left[\frac{(1 - \nu)Eu_x}{(1 + \nu)(1 - 2\nu)} + \frac{\nu E v_y}{(1 + \nu)(1 - 2\nu)} + \frac{\nu E w_z}{(1 + \nu)(1 - 2\nu)}\right. \\
&\left. - \frac{E\alpha\,\Delta T}{(1 - 2\nu)}\right] + \frac{\partial}{\partial z}\left[\frac{Eu_z}{2(1 + \nu)} + \frac{Ew_x}{2(1 + \nu)}\right] = 0 \qquad (4) \\
&\frac{\partial}{\partial x}\left[\frac{Eu_z}{2(1 + \nu)} + \frac{Ew_x}{2(1 + \nu)}\right] + \frac{\partial}{\partial z}\left[\frac{(1 - \nu)Ew_z}{(1 + \nu)(1 - 2\nu)}\right. \\
&\left. + \frac{\nu E u_x}{(1 + \nu)(1 - 2\nu)} + \frac{\nu E v_y}{(1 + \nu)(1 - 2\nu)} - \frac{E\alpha\,\Delta T}{1 - 2\nu}\right] = 0
\end{aligned}$$

The term $v_y$ in equation (4) is retained because the assumption $\epsilon_y = 0$ is more restrictive than necessary for plane strain (Ref. 13). Therefore, provision for retraining $\epsilon_y$ as an assumed value of

substructure strain only, is included in the equilibrium and stress equations for plane strain.

Since the ablation material is rigidly bonded to the substructure, the boundary conditions at the interface are

$$u = \alpha_s \Delta T_s x, \quad w = 0 \quad \text{on} \quad 0 \leq x \leq b, \quad z = 0 \tag{5}$$

The stress boundary conditions yield

$$\left.\begin{aligned} &(1 - \nu)u_x + \nu\epsilon_y + \nu w_z - (1 + \nu)\alpha\,\Delta T = 0 \\ &u_z + w_x = 0 \end{aligned}\right\} \begin{aligned} &x = b \\ &0 \leq z \leq h \end{aligned} \tag{6}$$

$$\left.\begin{aligned} &\nu u_x + \nu\epsilon_y + (1 - \nu)w_z - (1 + \nu)\alpha\,\Delta T = 0 \\ &u_z + w_x = 0 \end{aligned}\right\} \begin{aligned} &0 \leq x \leq b \\ &z = h \end{aligned} \tag{7}$$

The boundary conditions for the corners at $x = 0$, $z = h$, and $x = b$, $z = h$ are

$$\left.\begin{aligned} &u = 0 \\ &\nu u_x + \nu\epsilon_y + (1 - \nu)w_z - (1 + \nu)\alpha\,\Delta T = 0 \\ &u_z + w_x = 0 \end{aligned}\right\} \begin{aligned} &x = 0 \\ &z = h \end{aligned} \tag{8}$$

$$\left.\begin{aligned} &(1 - \nu)u_x + \nu\epsilon_y + \nu w_z - (1 + \nu)\alpha\,\Delta T = 0 \\ &\nu u_x + \nu\epsilon_y + (1 - \nu)w_z - (1 + \nu)\alpha\,\Delta T = 0 \\ &u_z + w_x = 0 \end{aligned}\right\} \begin{aligned} &x = b \\ &z = h \end{aligned} \tag{9}$$

Equations (4) are integrated by finite differences. Thus the x-z plane is subdivided by a rectilinear mesh (see Fig. 5) with a

constant mesh width $\Delta x$ in the x-direction and a constant mesh width $\Delta z$ in the z-direction. Mesh spacing with $\Delta x \neq \Delta z$ is used because the structures being analyzed typically have much larger dimensions in the x-direction than in the z-direction. The mesh lines are parallel to the coordinate axes with mesh lines on the edges $x = b$ and $z = h$.

The digital computer used to solve the finite difference equations did not permit the use of zero as a subscript. Therefore, the mesh points $x_m$ and $z_n$ are defined by

$$x_m = (m - 1)\Delta x, \quad m = 1,2,\ldots,I; \quad z_n = (n - 1)\Delta z, \quad n = 1,2,\ldots,J \tag{10}$$

## 2.3 Finite Difference Form of Equilibrium Equations

The method used to integrate the differential equations of equilibrium by means of finite differences is given in Appendix A. A digital computer program for solving the finite difference equations was written as part of this investigation. This computer program is discussed in Appendix B. A summary of the finite difference equations is presented in this section. Refer to Figure 5 for locations. For programing the finite difference equations for computer solution, the designations A, B, C, and D are used for recurring combinations of Poisson's ratio. Although this analysis assumes plane strain, plane stress solutions may be obtained from the computer program by using different values for A, B, C, and D. These constants for both plane strain and plane stress are given in Table I of Appendix A.

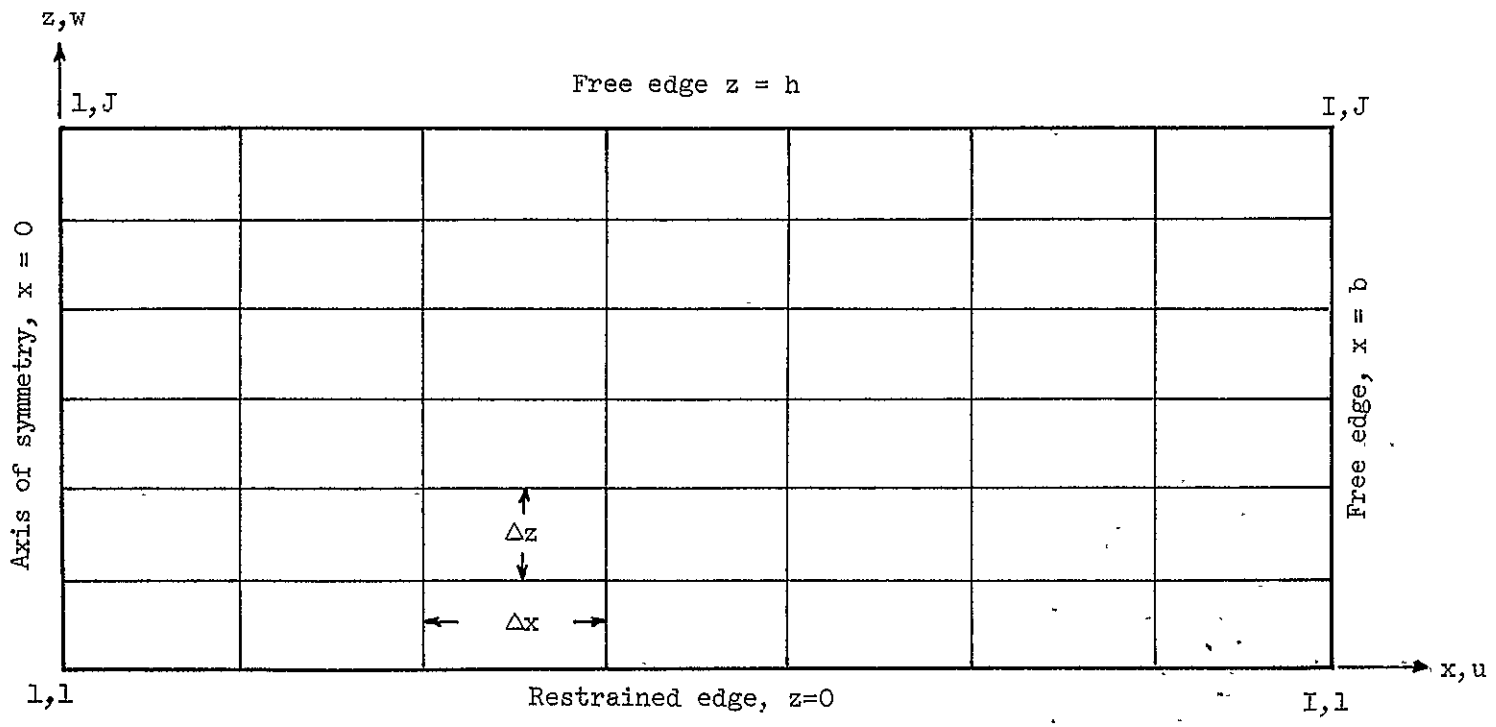


Figure 5.– Rectilinear finite difference mesh on x–z analysis plane

2.3.1 Corner Point 1,1

$$u = 0$$
$$w = 0 \tag{11}$$

2.3.2 Axis of Symmetry $m = 1, \quad 2 \leq n \leq J - 1$

$$u = 0$$

$$\frac{\partial}{\partial z}(AEw_z + BE\epsilon_y + BEu_x - CE\alpha\,\Delta T) + \frac{\partial}{\partial x}(DEu_z + DEw_x) =$$

$$\frac{A}{\Delta z^2}\left[\frac{(E_n + E_{n+1})}{2}(w_{m,n+1} - w_{m,n-1}) - \frac{(E_n + E_{n-1})}{2}(w_{m,n} - w_{m,n-1})\right]$$

$$+ \frac{B}{2\Delta x\,\Delta z}\left[E_{n+1}u_{m+1,n+1} - E_{n-1}u_{m+1,n-1}\right] + \frac{B\epsilon_y}{2\Delta z}\left[E_{n+1} - E_{n-1}\right]$$

$$- \frac{C}{2\Delta z}\left[(E\alpha\,\Delta T)_{n+1} - (E\alpha\,\Delta T)_{n-1}\right] + \frac{DE_n}{2\Delta x\,\Delta z}\left[u_{m+1,n+1} - u_{m+1,n-1}\right]$$

$$+ \frac{DE_n}{\Delta x^2}\left[-2w_{m,n} + 2w_{m+1,n}\right] = 0 \tag{12}$$

2.3.3 Corner Point $m = 1, \quad n = J$

$$u = 0$$

$$\frac{\partial}{\partial z}(AEw_z + BE\epsilon_y + BEu_x - CE\alpha\ \Delta T) =$$

$$\frac{A}{3\Delta z^2}\left[-\frac{9(E_n + E_{n-1})}{2}(w_{m,n} - w_{m,n-1}) + \frac{(E_{n-1} + E_{n-2})}{2}(w_{m,n-1} - w_{m,n-2})\right]$$

$$+ \frac{B}{6\Delta x\ \Delta z}\left[-7E_n u_{m+1,n} - 12E_{n-1}u_{m+1,n-1} + 3E_{n-2}u_{m+1,n-2}\right]$$

$$+ \frac{B\epsilon_y}{6\Delta z}\left[-7E_n - 12E_{n-1} + 3E_{n-2}\right] - \frac{C}{6\Delta z}\left[-7(E\alpha\ \Delta T)_n\right.$$

$$\left. - 12(E\alpha\ \Delta T)_{n-1} + 3(E\alpha\ \Delta T)_{n-2}\right] = 0 \qquad (13)$$

2.3.4 Restrained Boundary $2 \le m \le I,\quad n = 1$

$$u = \alpha_s \Delta T_s x$$

$$w = 0$$

2.3.5 Interior $2 \le m \le I - 1,\quad 2 \le n \le J - 1$

$$\frac{\partial}{\partial x}(AEu_x + BE\epsilon_y + BEw_z - CE\alpha\ \Delta T) + \frac{\partial}{\partial z}(DEu_z + DEw_x) =$$

$$\frac{AE_n}{\Delta x^2}\left[u_{m-1,n} - 2u_{m,n} + u_{m+1,n}\right] + \frac{BE_n}{4\Delta x\ \Delta z}\left[w_{m+1,n+1} - w_{m+1,n-1}\right.$$

$$\left. - w_{m-1,n+1} + w_{m-1,n-1}\right] + \frac{D}{4\Delta x\ \Delta z}\left[E_{n+1}(w_{m+1,n+1} - w_{m-1,n+1})\right.$$

$$\left. - E_{n-1}(w_{m+1,n-1} - w_{m-1,n-1})\right] + \frac{D}{\Delta z^2}\left[\frac{(E_n + E_{n+1})}{2}(u_{m,n+1}\right.$$

$$\left. - u_{m,n}) - \frac{(E_n + E_{n-1})}{2}(u_{m,n} - u_{m,n-1})\right] = 0 \qquad (14a)$$

$$\frac{\partial}{\partial z}(AEw_z + BEu_x + BE\epsilon_y - CE\alpha\,\Delta T) + \frac{\partial}{\partial x}(DEu_z + DEw_x) =$$

$$\frac{A}{\Delta z^2}\left[\frac{(E_{n+1} + E_n)}{2}(w_{m,n+1} - w_{m,n}) - \frac{(E_n + E_{n-1})}{2}(w_{m,n} - w_{m,n-1})\right]$$

$$+ \frac{B}{4\Delta x\,\Delta z}\left[E_{n+1}(u_{m+1,n+1} - u_{m-1,n+1}) - E_{n-1}(u_{m+1,n-1} - u_{m-1,n-1})\right]$$

$$+ \frac{BE\epsilon_y}{2\Delta z}\left[E_{n+1} - E_{n-1}\right] - \frac{C}{2\Delta z}\left[(E\alpha\,\Delta T)_{n+1} - (E\alpha\,\Delta T)_{n-1}\right]$$

$$+ \frac{DE_n}{4\Delta x\,\Delta z}\left[u_{m+1,n+1} - u_{m-1,n+1} - u_{m+1,n-1} + u_{m-1,n-1}\right]$$

$$+ \frac{DE_n}{\Delta x^2}\left[w_{m-1,n} - 2w_{m,n} + w_{m-1,n}\right] = 0 \qquad (14b)$$

2.3.6 Exterior Boundary $2 \le m \le I - 1, \quad n = J$

$$\frac{\partial}{\partial x}(AEu_x + BE\epsilon_y + BEw_z - CE\alpha\,\Delta T) + \frac{\partial}{\partial z}(DEu_z + DEw_x) =$$

$$\left(A - \frac{B^2}{A}\right)\frac{E_n}{\Delta x^2}\left[u_{m-1,n} - 2u_{m,n} + u_{m+1,n}\right] + \frac{D}{3\Delta z^2}\left[-\frac{9(E_n + E_{n-1})}{2}\right.$$

$$\left.(u_{m,n} - u_{m,n-1}) + \frac{(E_{n-1} + E_{n-2})}{2}(u_{m,n-1} - u_{m,n-2})\right]$$

$$+ \frac{D}{12\Delta x\,\Delta z}\left[-7E_n(w_{m+1,n} - w_{m-1,n}) - 9E_{n-1}(w_{m+1,n-1} - w_{m-1,n-1})\right.$$

$$\left. + 3E_{n-2}(w_{m+1,n-2} - w_{m-1,n-2})\right] = 0 \qquad (15a)$$

$$\frac{\partial}{\partial z}(AEw_z + BEu_x + BE\epsilon_y - CE\alpha\ \Delta T) =$$

$$\frac{A}{3\Delta z^2}\left[-\frac{9(E_n + E_{n-1})}{2}(w_{m,n} - w_{m,n-1}) + \frac{(E_{n-1} + E_{n-2})}{2}(w_{m,n-1} - w_{m,n-2})\right]$$

$$+ \frac{B}{12\Delta x\ \Delta z}\left[-7E_n(u_{m+1,n} - u_{m-1,n}) - 12E_{n-1}(u_{m+1,n-1} - u_{m-1,n-1})\right.$$

$$\left. + 3E_{n-2}(u_{m+1,n-2} - u_{m-1,n-2})\right] + \frac{B\epsilon_y}{6\Delta z}\left[-7E_n - 12E_{n-1} + 3E_{n-2}\right]$$

$$- \frac{C}{6\Delta z}\left[-7(E\alpha\ \Delta T)_n - 12(E\alpha\ \Delta T)_{n-1} + 3(E\alpha\ \Delta T)_{n-2}\right] = 0 \qquad (15b)$$

2.3.7 Exterior Boundary $m = I,\ 2 \le n \le J - 1$

$$\frac{\partial}{\partial x}(AEu_x + BE\epsilon_y + BEw_z - CE\alpha\ \Delta T) =$$

$$\frac{A}{3\Delta x^2}\left[-9u_{m,n} + 10u_{m-1,n} - u_{m-2,n}\right] + \frac{BE_n}{12\Delta x\ \Delta z}\left[-7(w_{m,n+1} - w_{m,n-1})\right.$$

$$\left. -12(w_{m-1,n+1} - w_{m-1,n-1}) + 3(w_{m-2,n+1} - w_{m-2,n-1})\right]$$

$$- \frac{8}{3\Delta x}BE_n\epsilon_y + \frac{8}{3\Delta x}C(E\alpha\ \Delta T)_n = 0 \qquad (16a)$$

$$\frac{\partial}{\partial z}(AEw_z + BEu_x + BE\epsilon_y - CE\alpha\,\Delta T) + \frac{\partial}{\partial x}(DEu_z + DEw_x) =$$

$$\left(A - \frac{B^2}{A}\right)\frac{1}{\Delta z^2}\left[\frac{(E_n + E_{n+1})}{2}(w_{m,n+1} - w_{m,n}) - \frac{(E_n + E_{n-1})}{2}(w_{m,n} - w_{m,n-1})\right]$$

$$+ \frac{DE_n}{3\Delta x^2}\left[-9w_{m,n} + 10w_{m-1,n} - w_{m-2,n}\right] + \frac{DE_n}{12\Delta x\,\Delta z}\left[-7(u_{m,n+1} - u_{m,n-1})\right.$$

$$\left. - 12(u_{m-1,n+1} - u_{m-1,n-1}) + 3(u_{m-2,n+1} - u_{m-2,n-1})\right]$$

$$- \frac{C}{2\Delta z}\left(1 - \frac{B}{A}\right)\left[(E\alpha\,\Delta T)_{n+1} - (E\alpha\,\Delta T)_{n-1}\right]$$

$$+ \frac{B\epsilon_y}{2\Delta z}\left(1 - \frac{B}{A}\right)\left[E_{n+1} - E_{n-1}\right] = 0 \qquad (16b)$$

2.3.8 Corner Point m = I, n = J

$$\frac{\partial}{\partial x}(AEu_x + BE\epsilon_y + BEw_z - CE\alpha\,\Delta T) =$$

$$\left(A - \frac{B^2}{A}\right)\frac{E_n}{3\Delta x^2}\left[-9u_{m,n} + 10u_{m-1,n} - u_{m-2,n}\right]$$

$$+ \frac{8}{3\Delta x}\left(A - \frac{B^2}{A}\right)\left[-\frac{BE_n\epsilon_y + C(E\alpha\,\Delta T)_n}{A + B}\right] = 0 \qquad (17a)$$

$$\frac{\partial}{\partial z}(AEw_z + BEu_x + BE\epsilon_y - CE\alpha\,\Delta T) =$$

$$\left(A - \frac{B^2}{A}\right)\frac{1}{3\Delta z^2}\left[-\frac{9(E_n + E_{n-1})}{2}(w_{m,n} - w_{m,n-1}) + \frac{(E_{n-1} + E_{n-2})}{2}\right.$$

$$\left.(w_{m,n-1} - w_{m,n-2})\right] - \left(1 - \frac{B}{A}\right)\frac{B\epsilon_y}{2\Delta z}\left[3E_n - 4E_{n-1} + E_{n-2}\right.$$

$$+ C\left(\frac{B}{A} - 1\right)\frac{1}{2\Delta z}\left[3(E\alpha\,\Delta T)_n - 4(E\alpha\,\Delta T)_{n-1} + (E\alpha\,\Delta T)_{n-2}\right]$$

$$+ \frac{8}{3\Delta z}\left(A - \frac{B^2}{A}\right)\left[-\frac{BE_n\epsilon_y + C(E\alpha\,\Delta T)_n}{A + B}\right] = 0 \qquad (17b)$$

# CHAPTER III

# EXPERIMENTAL TEST PROGRAM

A test program of limited scope was conducted to investigate the behavior of ablation materials subjected to restrained shrinkage. Eight small models consisting of rectangular panels of ablation material bonded to steel substructures were tested in a cryochamber at the Langley Research Center.

## 3.1 Model Configuration

The model configuration is shown in Figure 6. The models were fabricated by bonding two 4- by 11-inch ablation material panels to a 0.080-inch-thick steel plate. The steel plate was made wider than the ablation material panels to provide a means to mount the model in the cryochamber. The planform area of the model was necessarily much smaller than an actual heat shield, but the ablation material thickness was full scale. A symmetrical model was used to eliminate bending. The model substructure was sandwiched between two ablation material panels which were both cooled simultaneously. The model substructure provided an extensional stiffness similar to an actual structure. This model configuration furnished a shrinkage restraint boundary condition on one surface of the ablation material and stress free boundaries on all other surfaces. These boundary conditions simulate those of an actual heat shield and agree with those assumed in the analysis. To indicate ablation material cracking during the tests, crack detection circuits of conducting paint

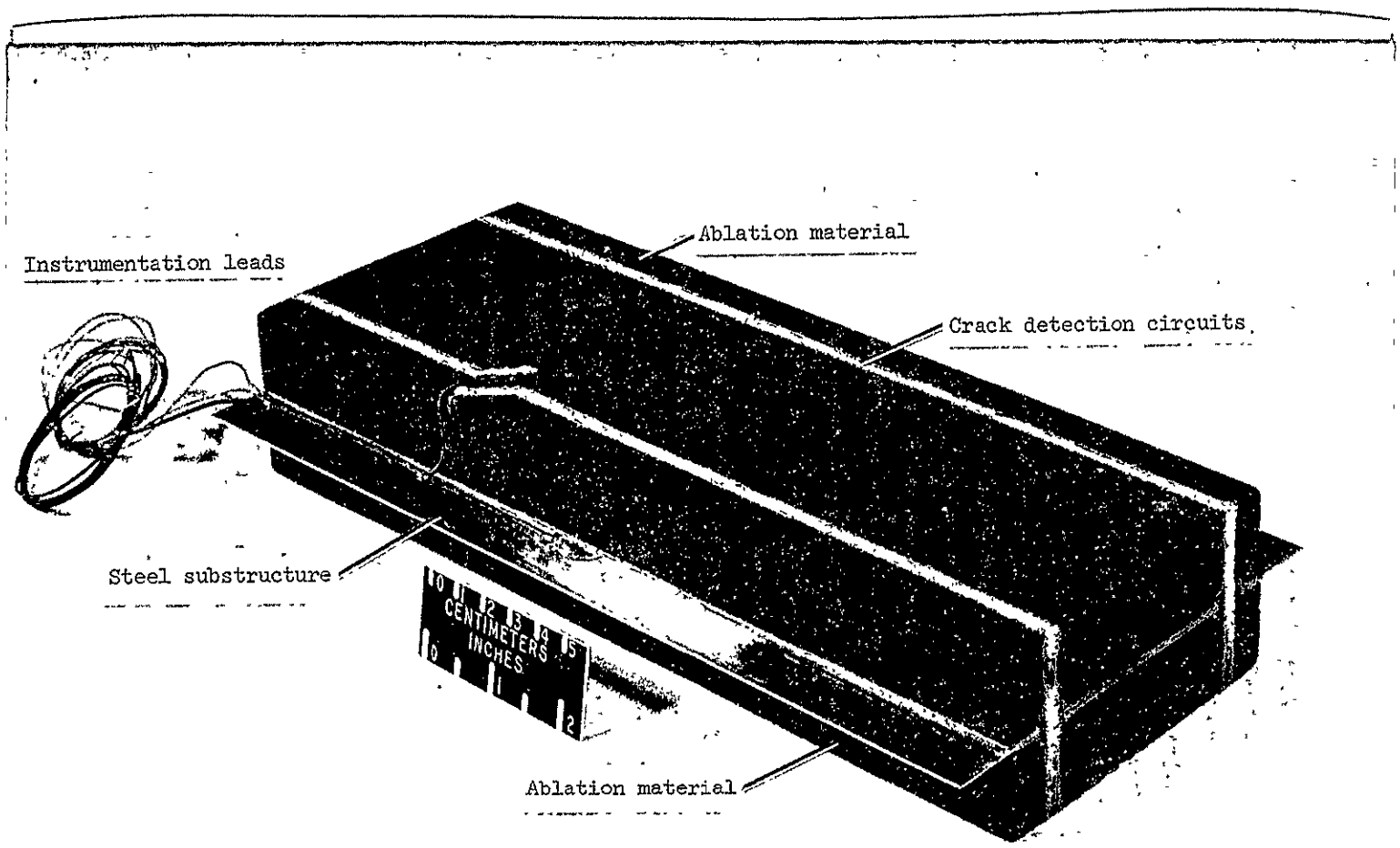


Figure 6.– Test model configuration

were applied to the model surfaces. These crack detectors are visible in Figure 6. The models were also instrumented with thermocouples to measure the temperature of the ablation material and substructure during testing. Neither the thin layer of conducting paint nor the thermocouples bonded into the ablation material appeared to have any physical influence on the cracking of the ablation material during the tests.

### 3.2 Ablation Material

Six models were fabricated with the ablation material shown in Figure 6. This material is a low density composite of nylon and phenolic which has been widely tested as an ablation material (Ref. 14) and is typical of the materials considered for ablative panels on future manned spacecraft. The phenolic nylon material was tested at thicknesses of 1/4, 5/8, and 1 inch. Three models were bonded with an adhesive having a cure temperature of 325° F and the other three were bonded with a room temperature curing adhesive. Both adhesives are commonly used in heat-shield fabrication, particularly the high temperature curing adhesive. The thermophysical properties of the phenolic nylon test material are reported in Reference 10. Data from Reference 10[1] which are pertinent to this investigation are shown in Figures 7 and 8. The faired curves shown in these figures are also from Reference 10. These data show large variations and indicate uncertainties in derived strength properties. Such variations in data

[1]These data are presented with the written permission of the authors.

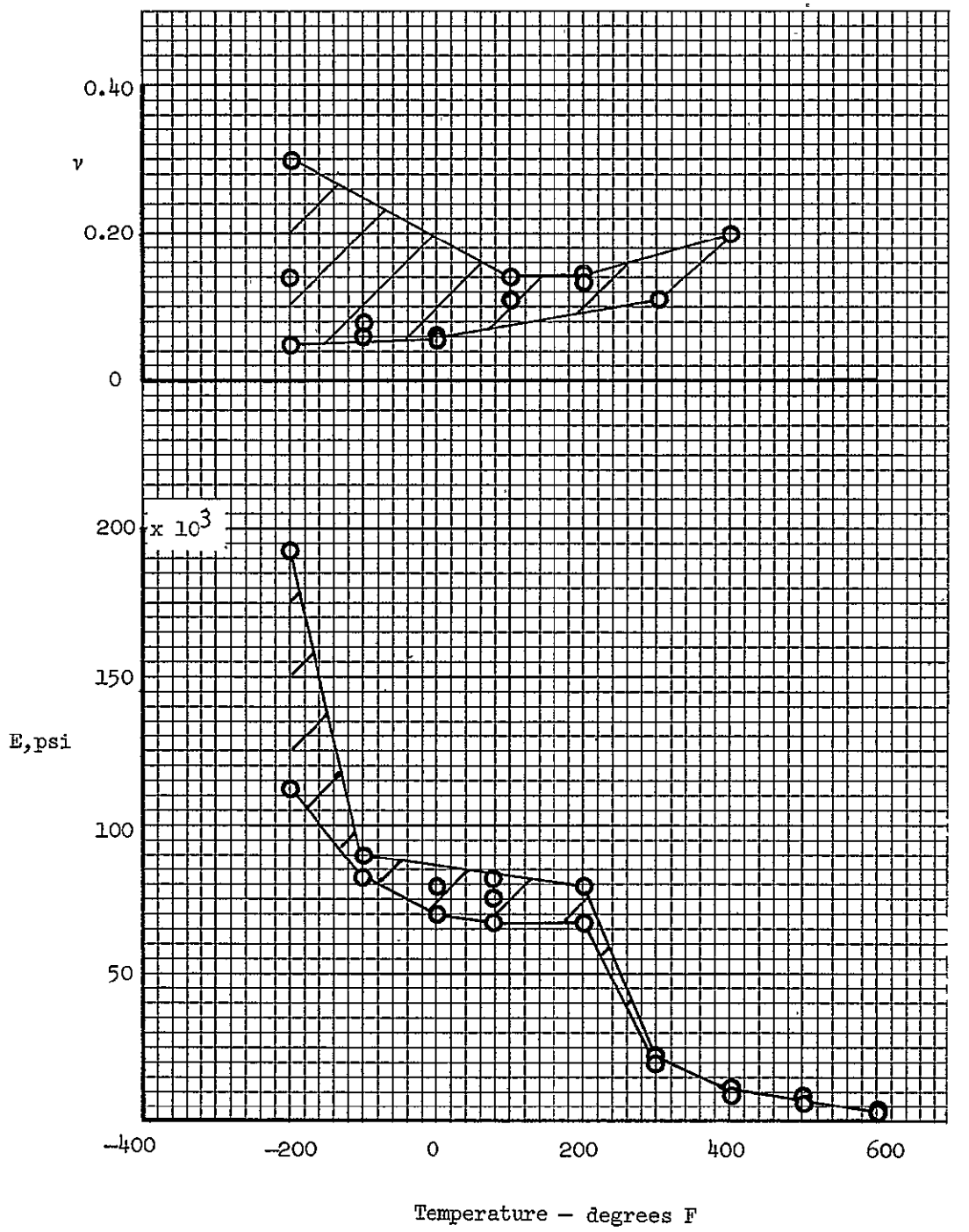


Figure 7.– Elastic modulus and Poisson's ratio versus temperature for phenolic–nylon ablation material loaded in tension (data from ref. 10)

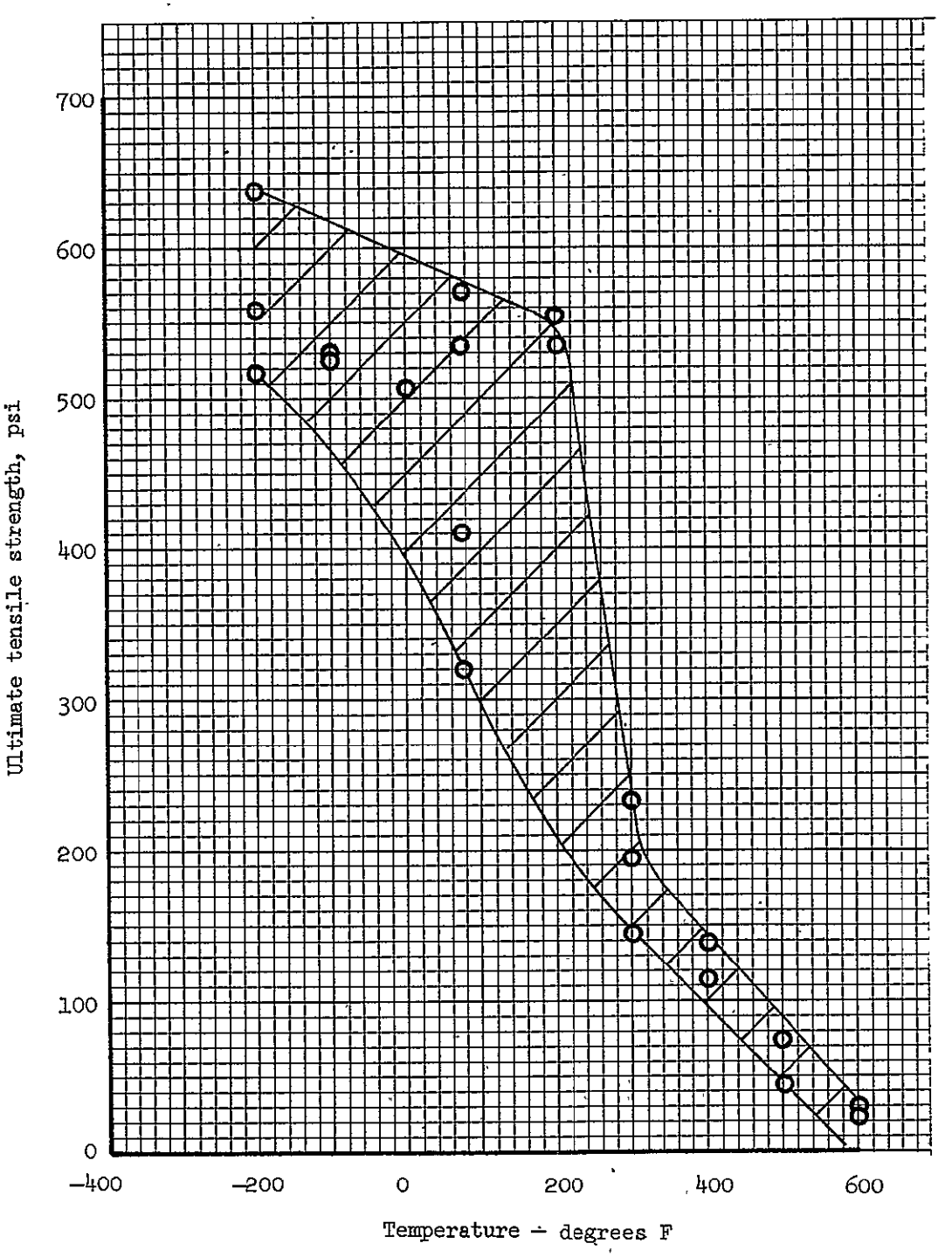


Figure 8.– Ultimate tensile strength versus temperature for phenolic–nylon ablation material (data from ref. 10)

are typical for ablation materials. Phenolic nylon ablation material also exhibits dimensional instability when subjected to changes in humidity. The constituent materials are hydroscopic and will absorb atmospheric moisture which produces swelling. Exposure to vacuum will cause the material to lose moisture and shrink.

Of the remaining two models, one was fabricated with NASA 602 and one with the Apollo spacecraft ablation material. NASA 602 is a silicone elastomer material described in Reference 1. This material differs from phenolic nylon in composition and is less brittle at room temperature, but has a coefficient of thermal expansion which is about twice as large as phenolic nylon. A 1-inch thickness of NASA 602 was tested and it was bonded to the substructure by using the constituent silicone resin as an adhesive. The Apollo heat-shield material is an epoxy-based composite reinforced with a plastic honeycomb. Heat shields of this material are fabricated by bonding the honeycomb to the spacecraft structure and then filling the honeycomb cells with ablation material. The resulting ablative shield consists of many small columns of ablation material separated by honeycomb cell walls. A 1-inch thickness of the Apollo material was tested to compare its behavior to the phenolic nylon.

## 3.3 Test Procedures

The models were tested in a cylindrical vacuum chamber whose walls contained liquid nitrogen. The models were supported in the test chamber so as to permit simultaneous radiation cooling of both

rectangular slabs of ablation material. The test procedure was as follows: The model was placed in the test chamber and the instrumentation was connected to recorders. Radiation shields consisting of fibrous insulation with an aluminum foil cover were placed over all exposed surfaces of the steel substructure and the model ends. Only the exterior surface of the two ablation material slabs was exposed to the cold chamber walls. The test chamber was sealed, evacuated to a pressure of about 1 torr, and liquid nitrogen was then introduced into the chamber walls.

# CHAPTER IV

# RESULTS AND DISCUSSION

The test program described in Chapter III was performed to obtain data from typical ablation materials which would identify the critical stress regions during restrained shrinkage and which could be qualitatively compared with the analytical stress analysis. The computer program developed for this investigation was used to calculate stresses caused by restrained shrinkage. These calculations have been compared with exact solutions. Comparisons between the calculations and the test data have also been made. The results of these studies are presented and discussed in the following sections.

## 4.1 Experimental Results

The phenolic nylon plate models described in Chapter III are shown after testing in Figure 9. The models shown in Figures 9(a) and 9(b) had the steel substructure sandwiched between two 1/4-inch thicknesses of ablation material. These models developed cracks at a surface temperature of -125° F and substructure temperature of -120° F. Thermal stress calculations, which are presented in a subsequent section, indicate that this cracking occurred in the region of maximum in-plane tension stress. Edge cracking was not observed.

Figure 9(c) shows the interface cracks across the narrow end of the 5/8-inch thick models. These models cracked at a surface temperature of 30° F and substructure temperature of 72° F.

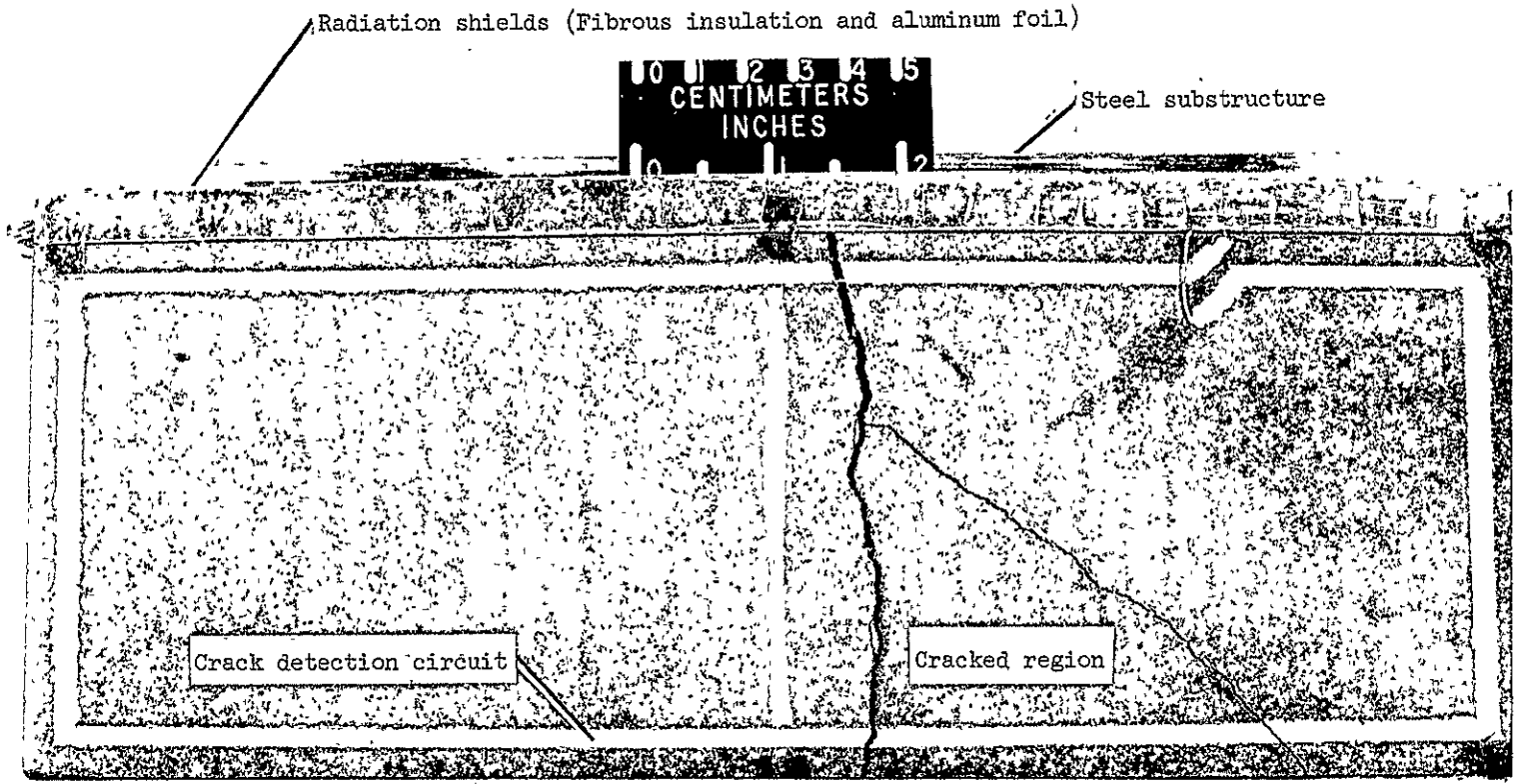


(a) Ablation material thickness of 1/4 in., bonded with room temperature curing adhesive

Figure 9.– Post test photographs of phenolic–nylon plate models

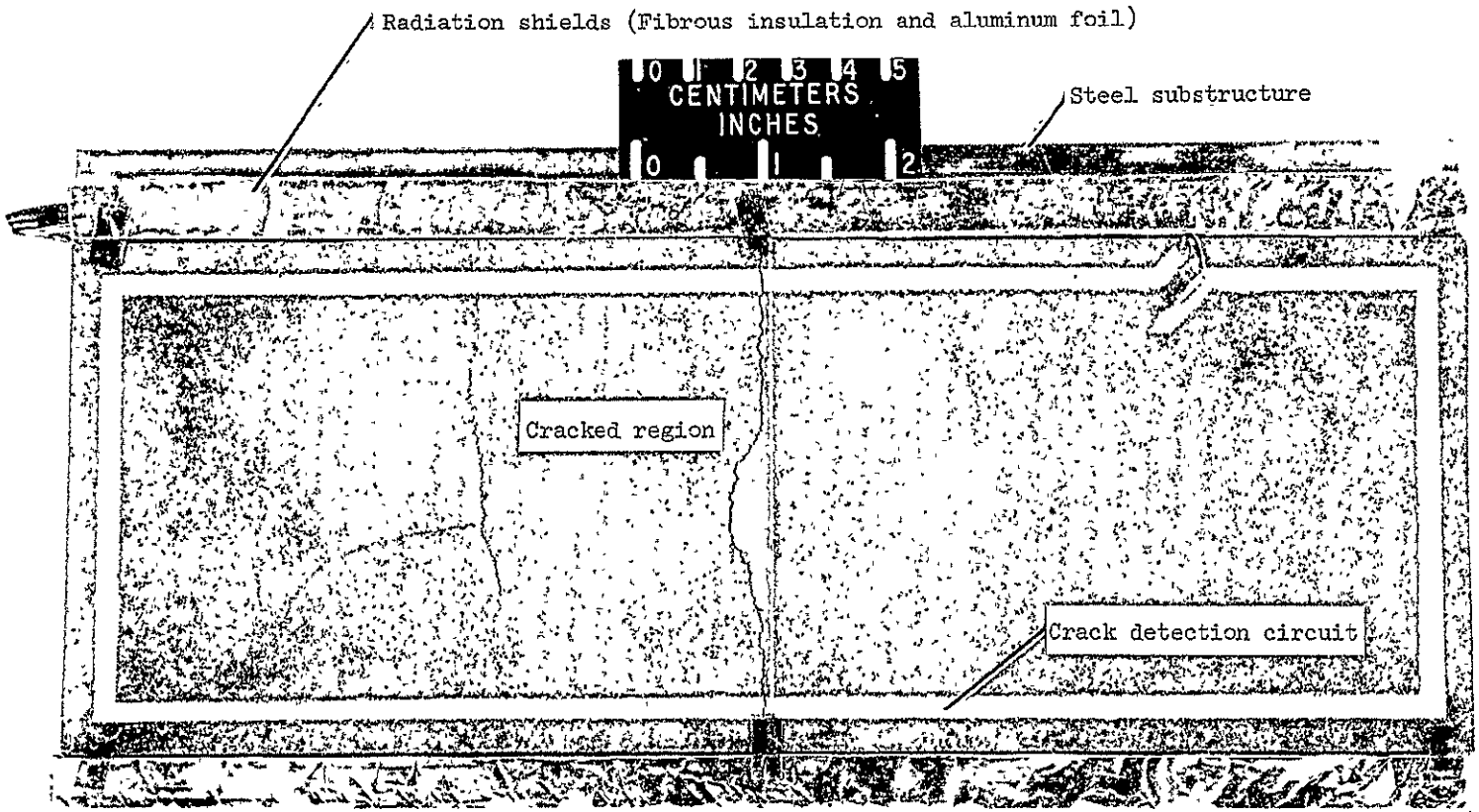


(b) Ablation material thickness of 1/4 in., bonded with high temperature curing adhesive

Figure 9.– Continued

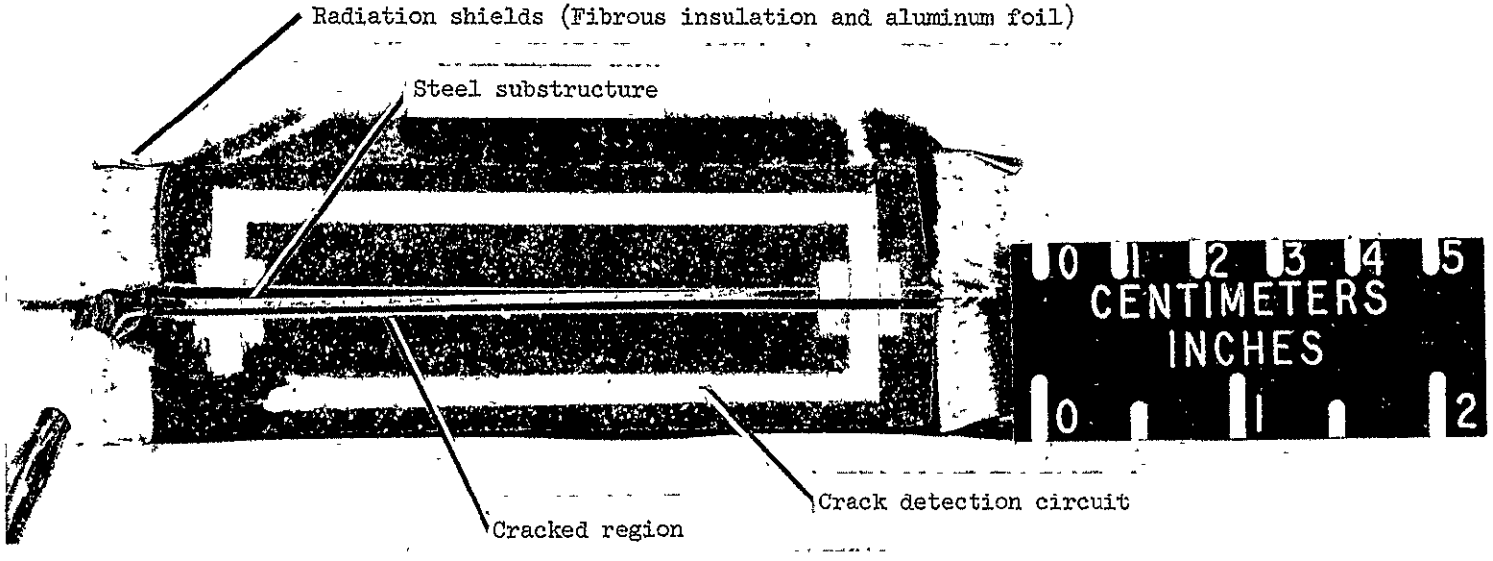


(c) Ablation material thickness of 5/8 in., bonded with room temperature curing adhesive

Figure 9.– Continued

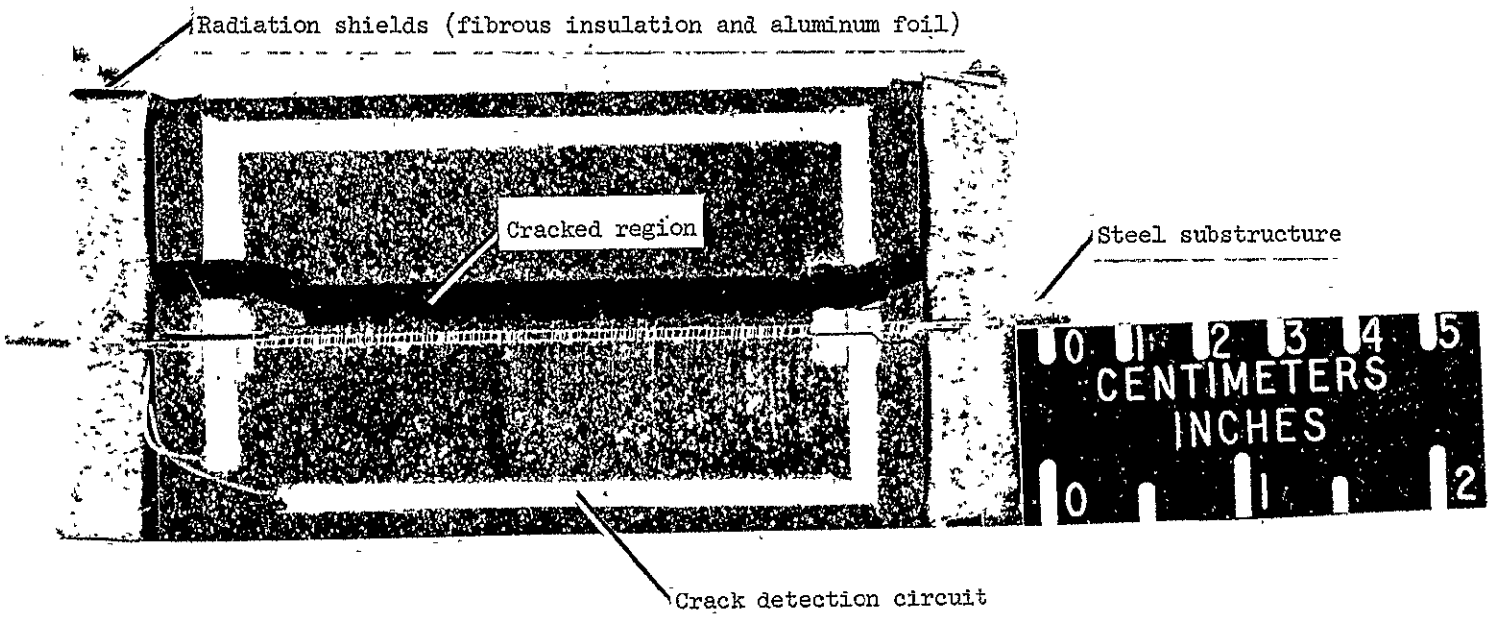


(d) Ablation material thickness of 1 in., bonded with high temperature adhesive

Figure 9.– Concluded

The crack location indicates that the cracking was caused by edge tension stresses. The cracked region of the models having 1-inch-thick ablation material is shown in Figure 9(d). The crack circuits indicated that these models developed end cracks while the test chamber was being evacuated prior to cooling. As discussed in Chapter III, phenolic nylon shrinks from moisture loss during vacuum exposure and this shrinkage produced edge stresses large enough to crack the ablation material. Subsequent cooling of the model to a surface temperature of -75° F increased the separation and caused the large crack visible in Figure 9(d).

The models with the ablation material bonded with high temperature curing adhesive performed essentially the same as those fabricated with a room temperature curing adhesive. The bonding operation at 325° F apparently did not cause significant thermal stress in the models. The reason for this is that the strength of this phenolic nylon material is extremely small at 325° F (see Figs. 7 and 8). Therefore, it is anticipated that the hot ablation material accommodated the differential contraction strains and did not develop significant thermal stresses during subsequent cooling to room temperature.

The test model fabricated with 1-inch-thick NASA 602 also developed end cracks at the location shown in Figure 9(d). The crack circuits did not function well with this material and, therefore, the temperature at cracking was not determined. This test result was expected and indicates that silicone elastomers are also subject to cracking from restrained shrinkage at low temperature. The model

fabricated with 1-inch-thick Apollo heat-shield material did not develop cracks during testing. This result was also expected because the honeycomb reinforcement is effective in preventing cracking due to restrained shrinkage.

## 4.2 Analysis Results

The accuracy of the numerical analysis is evaluated by comparing the calculated stresses with an exact solution. The exact case is the plane strain analysis of a semi-infinite slab with constant material properties. The slab is subjected to a uniform temperature change and is restrained in both the x- and y-directions such that the strain in these directions equals $\alpha_s \Delta T_s$. From Reference 15, the solution for this case (away from the edges) is $\sigma_x = \sigma_y = - E\alpha\, \Delta T/1 - \nu$, $\sigma_z = 0$ where $\alpha$ is the difference between the slab and substructure expansion coefficients.

Calculated stresses in the slab subjected to a uniform temperature decrease are shown in Figure 10. The stresses are normalized with respect to the parameter $E\alpha\, \Delta T/1 - \nu$ and the abscissa is the ratio of distance from the free edge to the slab thickness. As the distance from the free edge increases, the edge effects diminish and the calculated stresses agree with the exact solution in regions for which the exact solution is valid. Mesh spacings of $\Delta x = 0.125$ in. and $\Delta z = 0.025$ in. were used for all the calculations presented in this thesis.

The slab thermal stresses at the interface $z = 0$ are shown in Figure 10(a) and serious discrepancies exist between the calculated

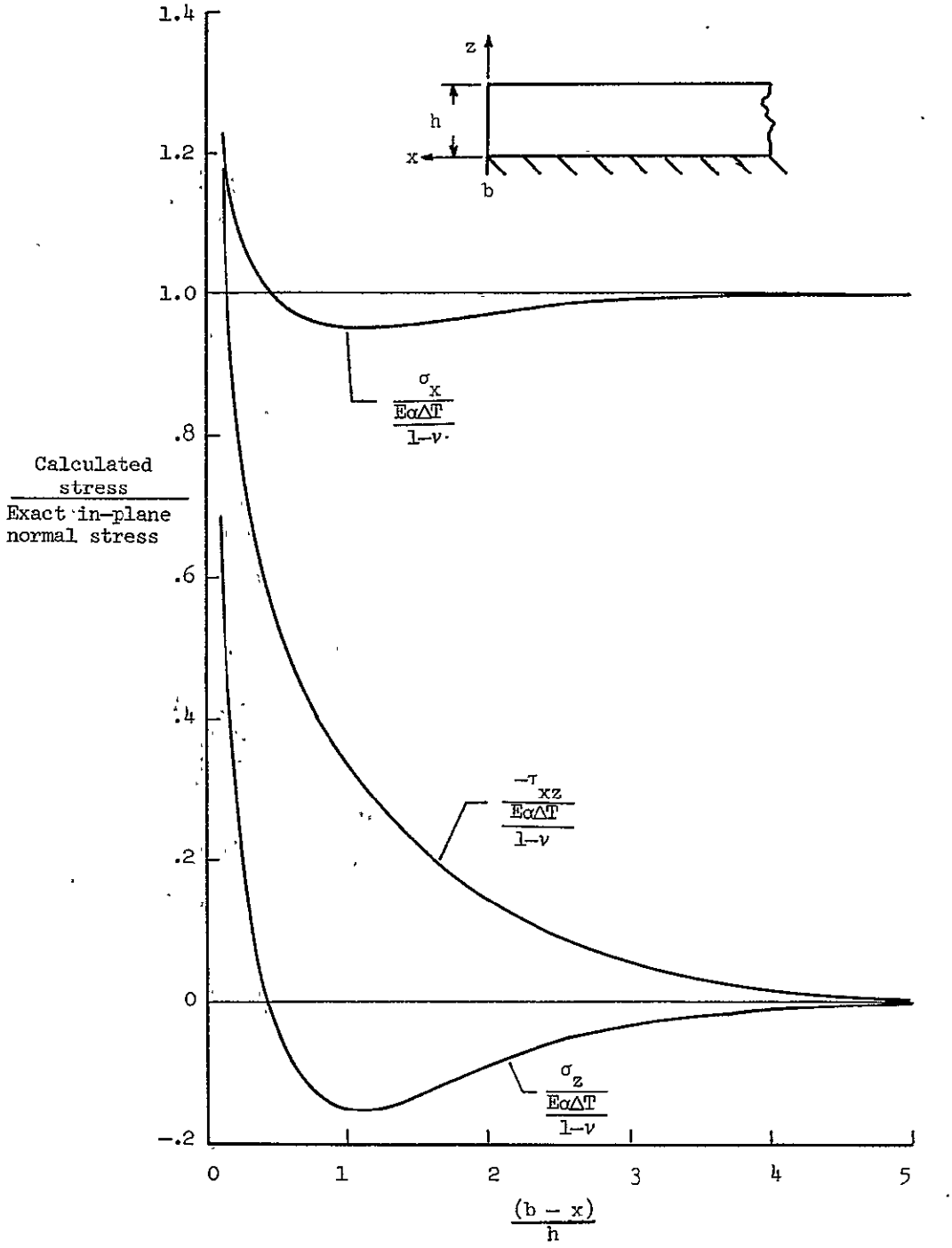


(a) Stress distribution at ablator–substructure interface, z = 0

Figure 10.– Calculated restrained shrinkage stresses for a uniform temperature slab

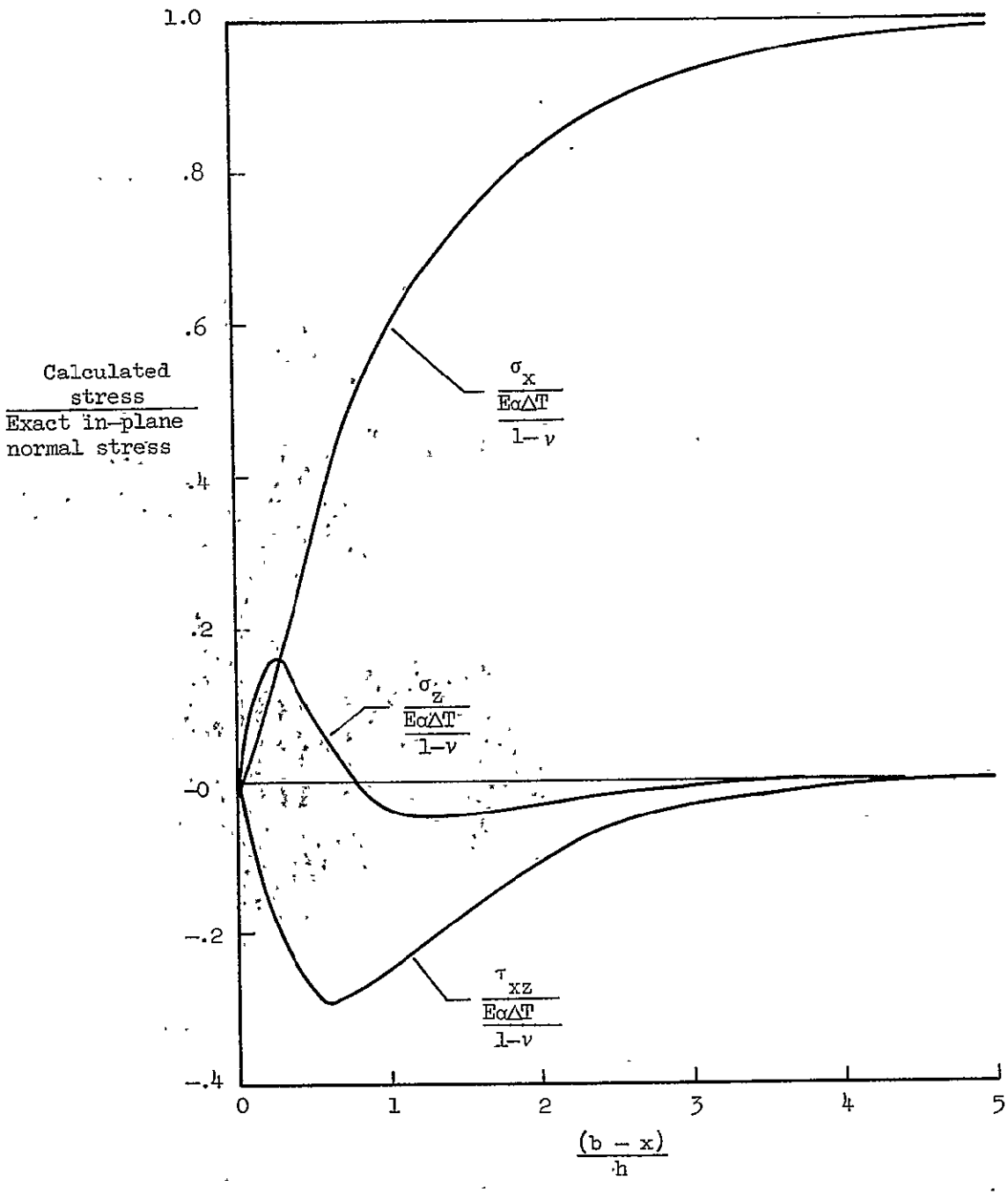


(b) Stress distribution at the slab mid-depth, $z = \frac{h}{2}$

Figure 10.– Continued

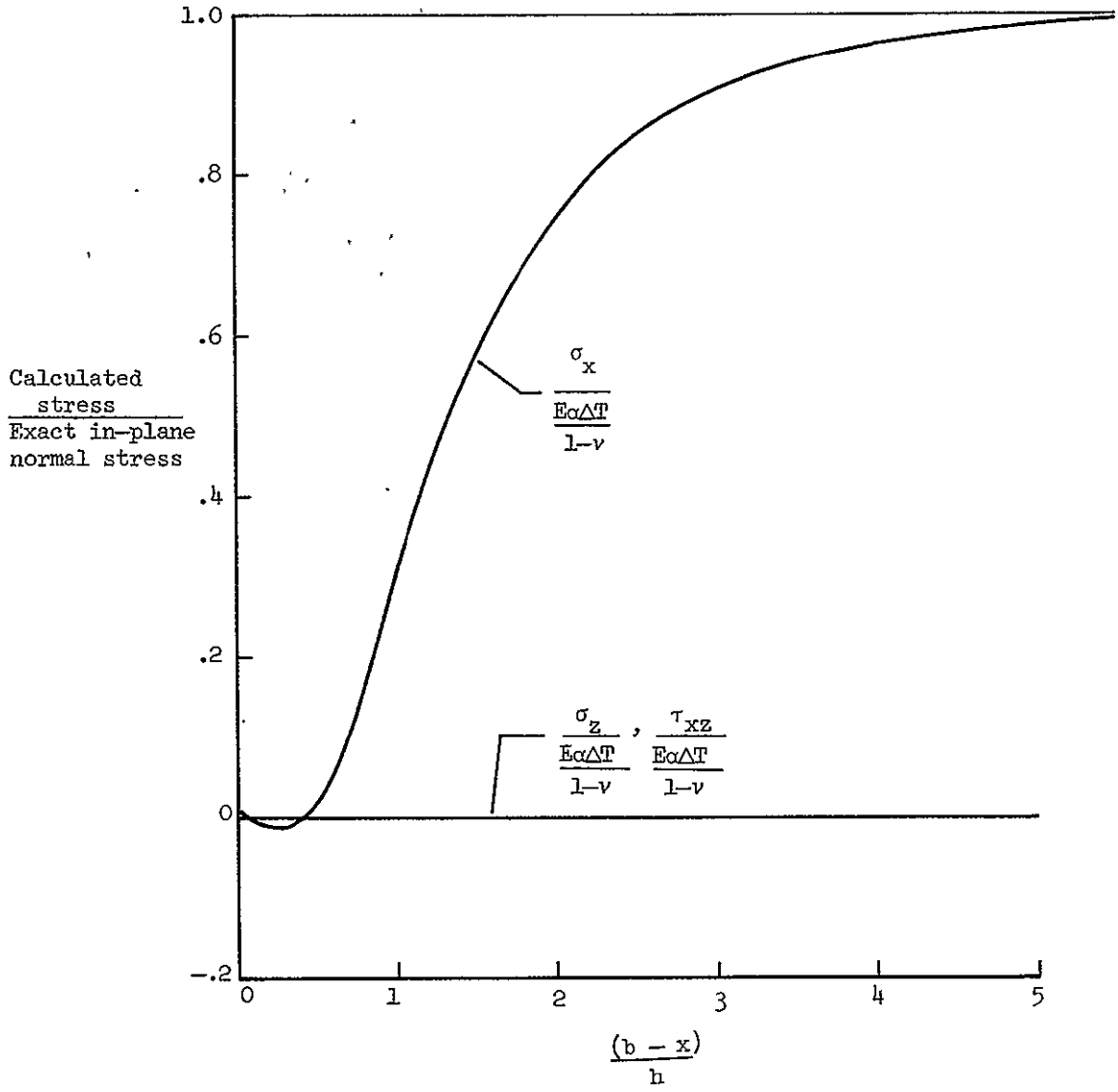


(c) Stress distribution at the slab surface, z = h

Figure 10.– Concluded

values and the free edge stress boundary conditions, $\sigma_x = \tau_{xz} = 0$, at $x = b$. This result was not anticipated and the analysis was completed before the results from the displacement analysis of Reference 8 were known. Much effort was spent in trying to resolve the difficulty, including the use of extremely small mesh spacings, but no successful solution was obtained. It is noted that corners are excluded in studies of finite difference approximations for mixed boundary-value problems (Refs. 16 and 17, for example). A stress singularity at the corner point is indicated by the large shear stress values obtained with the present analysis. The analysis of Reference 18 also identifies the corner point as a potential singularity point.

A stress singularity at the corner point, $x = b$, $z = 0$, means that the stresses at that point cannot be evaluated, but it does not invalidate the results obtained at other regions of the slab. It is emphasized that the singularity is one of stress, but not of displacements. With the present analysis, the interface displacements are specified as $u = \alpha_s \Delta T_s x$ and $w = 0$. These values for $u$ and $w$ also specify the values for $u_x$ and $w_x$. The interface displacements appear as known values in the equilibrium equations for the mesh points at $1 \leq m \leq I$, $n = 2$ and these displacements, therefore, are used in the systems of equations which are solved for $u$ and $w$ throughout the x-z plane. Since the interface displacements are known, however, the equilibrium equations are not applied at the interface. This means that the prescribed stresses at the corner point are not included in the slab displacement equations. The interface stresses are

calculated with the specified values for $u_x$ and $w_x$ and from values for $u_z$ and $w_z$ obtained with forward difference equations using the specified interface displacements and the calculated slab displacements. Since $w = w_x = 0$ is specified along the interface, satisfying the shear stress boundary condition requires that $u_z = 0$ at $x = b$, but this condition is not in the slab displacement equations. Since the slab contracts more than the restraining substructure, the $u$ displacements at the mesh points $I,2$ and $I,3$ are greater than $u_{I,1}$. The $u$ displacements at these three points do not lie along a parabolic curve. Therefore, a three point forward difference equation gives a negative and nonzero $u_z$. Decreasing the mesh spacing, $\Delta z$, merely increases the calculated value for $u_z$ at $x = b$. To satisfy the $\sigma_x = 0$ condition, with $u_x$ specified, requires negative values for $w_z$ which are considerably greater than the values at $x$ less than $b$. To satisfy the slab equilibrium equations along the $x = b$ edge of the x-z plane, however, $w_x$ must be positive at the mesh points for $n \geq 2$ because $u_z$ is negative at these points. Therefore, the forward difference equation does not give large negative values for $w_z$ at the corner point. The net result is that $\sigma_z$ at the corner point is a tension stress rather than the compression stress given by the free edge boundary conditions.

It is noted that for slab equilibrium, the sum of $\sigma_z$ stresses along the interface must be zero. The $\sigma_z$ stresses shown in Figure 10(a) satisfy this requirement, however, this does not indicate a unique solution. It is speculated, however, that even if compressive

$\sigma_z$ stresses exist at the corner point, a stress reversal must occur near the corner. In Reference 5 the author states that photoelasticity measurements up to 0.001 inch from the corner showed tension values for $\sigma_z$. The test results from the present investigation also indicate tension stresses as evidenced by the edge cracking at the interface.

The numerical plane-strain analysis gives stress distributions in the x-z plane which: (1) agree with the exact solution well away from the edges; (2) agree with the prescribed boundary stresses at the slab mid-depth and surface (Figs. 10(b) and 10(c)); and (3) qualitatively agree with the plane stress analyses of References 4 and 8 at the mid-depth and surface locations. In Reference 4, the author states that the effects of the stress singularity were highly local and that valid solutions were obtained away from the singularity. Because of (3) this statement can be applied to the present analysis. Also, the displacement equations are solved by repeated iterations of simultaneous equations and if significant perturbations were introduced by the corner effect then these perturbations would influence all displacements. Such perturbations would cause the calculated stresses in all regions of the x-z plane to diverge from exact solutions. Since this divergence does not occur, it is concluded that the corner effects are confined to the immediate vicinity of the corner and that valid stresses are calculated at other regions.

Figure 10(b) shows that at the mid-depth, $z = h/2$, of the restrained slab the edge stresses are minimal. Therefore, to investigate edge tension stresses which might cause the ablation material to

crack, it was necessary to select an edge region which was somewhat removed from the corner point, $x = b$, $z = 0$, and yet in the highly stressed region. A location at $z = 0.05$ inch was selected. At this location, good agreement was obtained with the prescribed boundary condition that $\sigma_x = 0$. The calculated shear stresses at this boundary location reached peak values near the edge and indicated a rapid decrease toward the prescribed edge value. Figure 11 shows the calculated values for $\sigma_z$, normalized with respect to $E\alpha\,\Delta T/1 - \nu$, for various thickness slabs subjected to a uniform temperature decrease. These values are calculated at $x = b$, $z = 0.05$ inch, and show that the edge tension stress increases with slab thickness. This result agrees with the experimental data presented herein.

In actual applications, an ablation heat shield would have a temperature gradient in the z-direction rather than the uniform temperature assumed in Figure 11. Therefore, the influence of three different temperature distributions on restrained thermal stresses was investigated. Case I assumed a uniform temperature distribution, Case II assumed a linear temperature distribution through the ablation material thickness with $\Delta T = 0$ at $z = 0$ and Case III assumed a uniform temperature in the upper half of the slab thickness ($h/2 \leq z \leq h$) and a parabolically increasing temperature to $\Delta T = 0$ at $z = 0$ in the lower half of the slab ($0 \leq z \leq h/2$). The value for $\Delta T$ at $z = h$ was the same for all three cases. The temperature distributions for Case II and Case III are suggested by the temperature distribution measured during model tests. The calculated stresses are

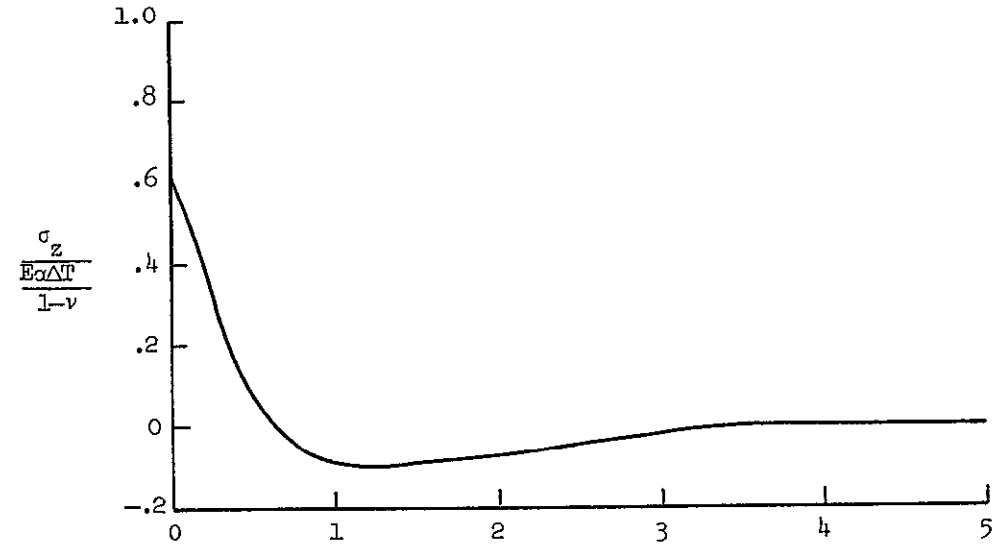


(a) h = 0.25 in.

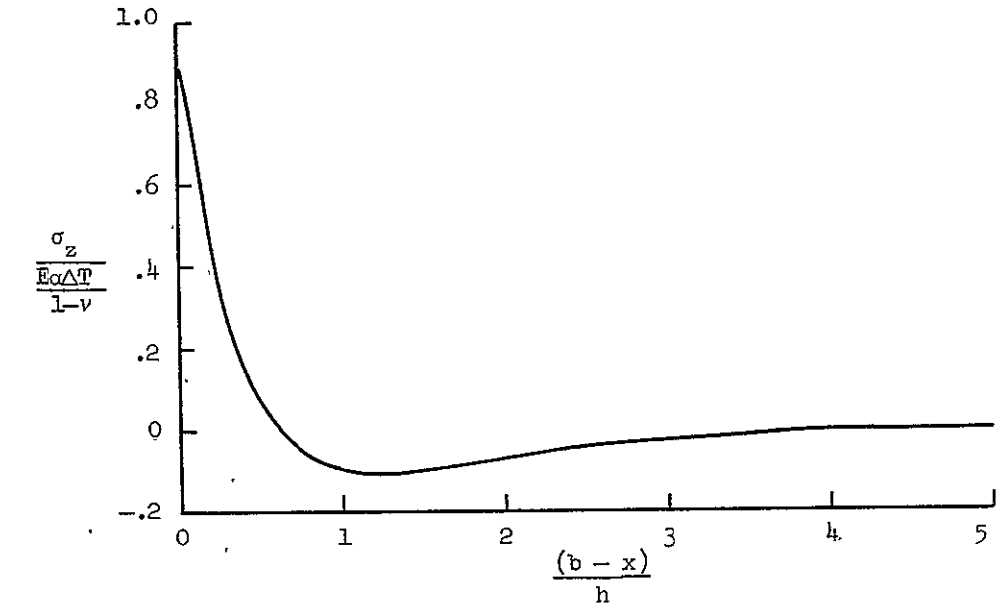


(b) h = 0.35 in.

Figure 11.– Calculated $\sigma_z$ stresses for various thickness slabs at z = 0.05 in. (slab subjected to restrained shrinkage at a uniform temperature)

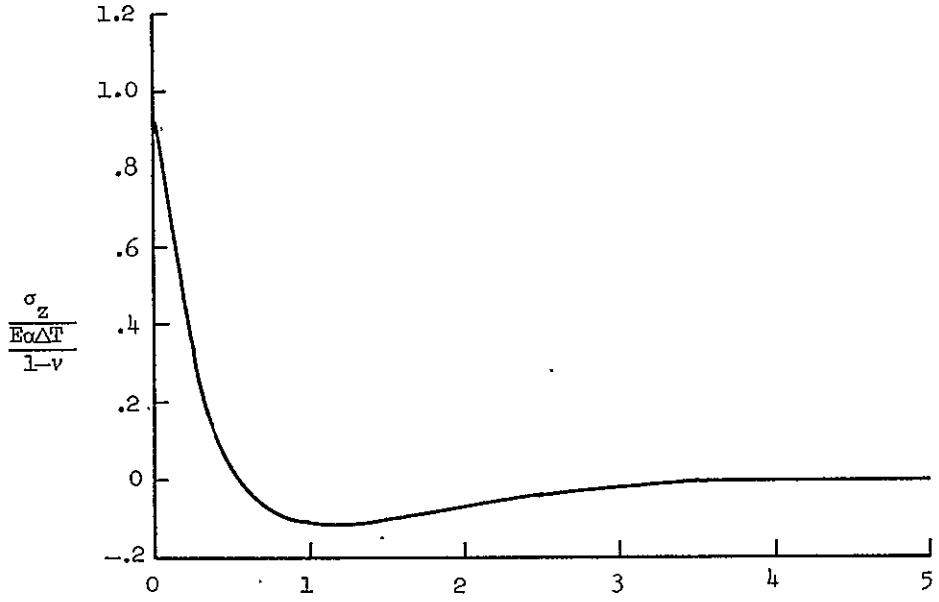


(c) h = 0.4 in.

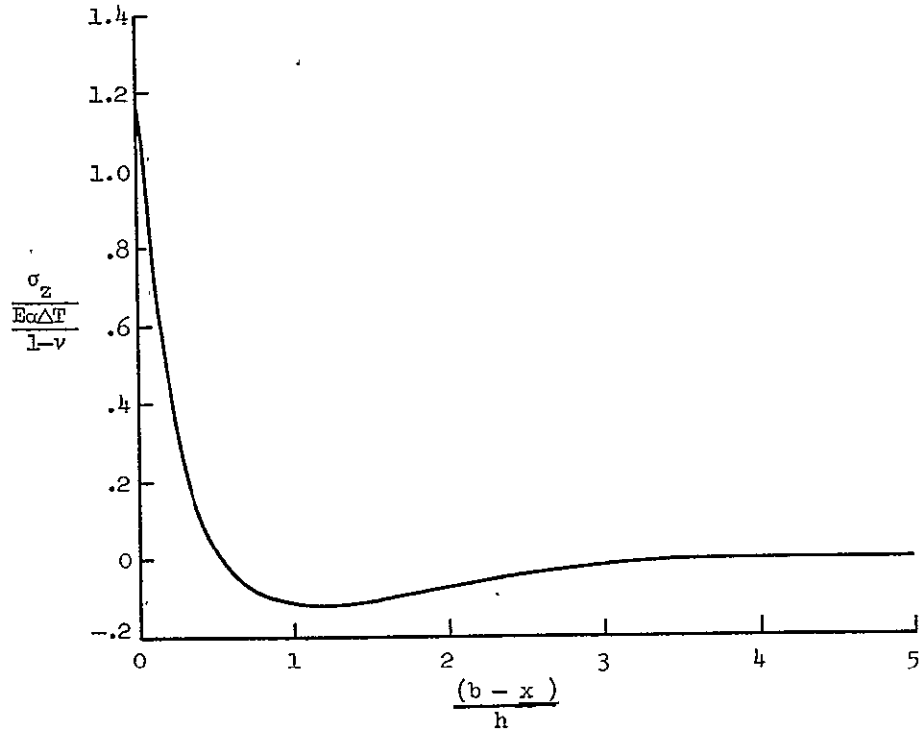


(d) h = 0.5 in.

Figure 11.– Concluded

compared in Figure 12 which shows the ratio of $\sigma_z$ at $x = b$, $z = 0.05$ inch to $\sigma_{x_{max}}$ for various assumed slab thicknesses.

Figure 12 shows that the edge tension stress increases with slab thickness for all three temperature distributions. The Case III temperature distribution induces the greatest slab curvature and causes the highest edge tension stress near the nonbending interface. As expected, the linear temperature distribution of Case II produced the lowest tension stress. The most interesting point about these calculations is the indication that the region of maximum tension stress shifts from the slab interior to the edge when the slab thickness exceeds about 0.5 inch. The calculations are consistent with the test results. Interior cracks developed in the test models with a slab thickness of 1/4 inch and Figure 12 shows a value of $\sigma_z/\sigma_{x_{max}}$ less than 1.0. The models with slab thickness of 5/8 and 1 inch developed edge cracks and the value of $\sigma_z/\sigma_{x_{max}}$ for these thicknesses is greater than 1.0.

## 4.3 Comparison of Calculations and Test Results

Thermal stresses were calculated for a phenolic nylon material at the temperature when model cracking occurred. The test data indicated that the model with 1/4-inch-thick ablation material (Fig. 9(a)) cracked when the surface temperature was -125° F and the substructure temperature was -120° F. The reference temperature was 80°. The material properties were obtained from data in Reference 10. These data indicate that at the measured temperature the thermal

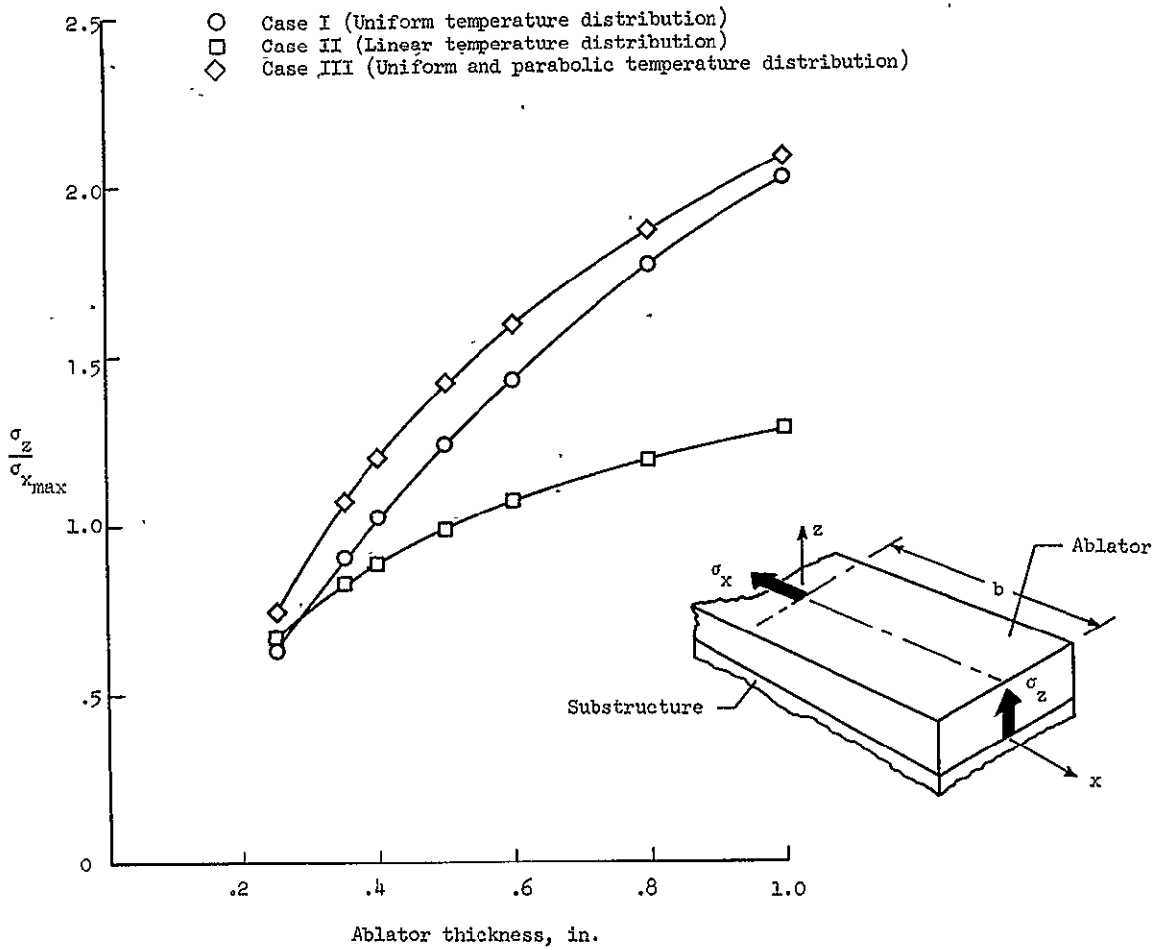


Figure 12.— The effects of various temperature distributions and slab thicknesses on the ratio of $\frac{\sigma_z}{\sigma_{x_{max}}}$ at x = b and z = 0.05 in.

expansion coefficient is $23.5 \times 10^{-6}$ in/in/deg F. However, as shown in Figure 7 the data for Poisson's ratio and Young's modulus show wide variations. The values selected were: $\nu = 0.1$ and $E = 120{,}000$ psi. The expansion coefficient for the steel substructure was taken as $6.76 \times 10^{-6}$ in/in/deg F. The thermal stress calculations indicated a maximum tension stress of 460 psi at the top surface of the ablation material. A calculation assuming Poisson's ratio equal to 0.25 produced a maximum stress of 550 psi. Examination of the ultimate tensile strength data in Figure 8 shows that these stress values would cause ablation material cracking such as occurred in the model tests.

Thermal stress calculations were also made for comparison with the 5/8-inch model (Fig. 9(c)). The model cracked at a surface temperature of $30^{\circ}$ F, a mid-depth temperature of $32^{\circ}$ F, and a substructure temperature of $72^{\circ}$ F. The reference temperature was $80^{\circ}$ F. The material properties were the same as previously discussed with the exception of Poisson's ratio which was assumed to be 0.15. The maximum tension stress occurred at the edge, but was only 150 psi, and well below the ultimate tension value from Figure 8. Apparently the stress resulting from moisture-loss shrinkage was primarily responsible for the model cracking and not the stress from the relatively small decrease in temperature.

# CHAPTER V

## CONCLUDING REMARKS

An approximate numerical analysis for restrained shrinkage stresses in rectangular slabs has been presented. Test results from rectangular slabs of ablation material subjected to severe restrained shrinkage have also been presented and qualitatively compared with analysis calculations. The present analysis which is programed for solution with a digital computer calculated restrained shrinkage stresses which are consistent with the test results reported herein and with other experimental investigations. The alternating direction technique (Ref. 19) which was programed to solve the finite difference equations appears to be rapid and efficient.

The analysis was an attempt to solve the mixed boundary-value problem of a rectangular plane having both specified displacement and stress boundary conditions. The analysis objective was not fully achieved because no satisfactory solutions were obtained at the boundary corner point for which both displacements and stresses were specified. The numerical analysis did not determine the strains and stresses at this boundary point with any precision. Extensive and time consuming efforts were made to improve the corner point solution, but these efforts were unsuccessful. It is not known what modifications to the analysis would be required to obtain better solutions.

Both the test results and the stress calculations from this investigation indicate that a heat shield subjected to restrained

shrinkage can develop edge separations between the ablation material and the substructure. Heat shields fabricated with bonded, unreinforced ablation materials appear susceptible to edge separation or cracking when the ablation material thickness exceeds about 0.5 inch. The data also indicate that this cracking may occur merely because of changes in the moisture content of the ablation material and at temperatures much less severe than those which could be encountered in space flight. The desirability of using honeycomb reinforced ablation material to withstand restrained shrinkage is evident, but must be weighed against fabrication cost and difficulty. A reinforced region at the heat-shield periphery might be an acceptable compromise solution.

REFERENCES


1. Laporte, A. H.: Research on Refurbishable Thermostructural Panels For Manned Lifting Entry Vehicles. NASA CR-638, November 1966.

2. Aleck, B. J.: Thermal Stresses in a Rectangular Plate Clamped Along an Edge. Journal of Applied Mechanics, June 1949.

3. Sundara Raja Iyengar, K. T.; and Alwar, R. A.: Thermal Stresses in a Long Rectangular Plate Constrained at One of the Shorter Edges. International Journal of Mechanical Science, December 1962.

4. Theocaris, P. S.; and Dafermos, K.: The Elastic Strip Under Mixed Boundary Conditions. Journal of Applied Mechanics, December 1964.

5. Durelli, A. J.; Parks, V. J.; and Bhodra, P.: Experimental Determination of Stresses and Strains in a Rectangular Plate Subjected to Biaxial Restrained Shrinkage. British Journal of Applied Physics, Vol. 17, December 1966.

6. Durelli, A. J.; Parks, V. J.; and del Rio, C. J.: Stresses in Square Slab Bonded on One Face to a Rigid Plate and Shrunk. Acta Mech., 3 (4), pp. 352-359, 1967.

7. Durelli, A. J.; and Parks, V. J.: Photoelastic Analysis in the Neighborhood of Corners of Long Strips Bonded on One Side and Shrunk. American Ceramic Society Bulletin 46 (6), pp. 582-586, June 1967.

8. Bauer, F.; and Reiss, E. L.: On the Numerical Determination of Shrinkage Stresses. IMM Report 371, Courant Institute of Mathematical Sciences, September 1968.

9. Wilson, R. G. (Compiler): Thermophysical Properties of Six Charring Ablators From 140° to 700° K and Two Chars From 800° to 3000° K. NASA TND-2991, October 1965.

10. Engelke, W. T.; Pyron, C. M., Jr.; and Pears, C. D.: Thermophysical Properties of a Low Density Phenolic Nylon Ablation Material. NASA CR-809, July 1967.

11. Swann, R. T.; Pittman, C. M.; and Smith, J. C.: One-Dimensional Numerical Analysis of the Transient Response of Thermal Protection Systems. NASA TND-2976, 1965.

12. Timoshenko, S. P.; and Goodier, J. N.: Theory of Elasticity, 2nd Ed. McGraw-Hill Book Company, New York, 1951.

13. Zudans, Z.; Yen, T. C.; and Steigelmann, W. H.: Thermal Stress Techniques in the Nuclear Industry. American Elsevier Publishing Company, New York, N. Y., 1965.

14. Dow, M. B.; Bush, H. G.; and Tompkins, S. S.: Analysis of the Supercircular Reentry Performance of a Low Density Phenolic Nylon Ablator. NASA TMX-1577, 1968.

15. Gatewood, B. E.: Thermal Stresses. McGraw-Hill Book Company, New York, 1957.

16. Forsythe, G. E.; and Wasow, W. R.: Finite-Difference Methods For Differential Equations. John Wiley and Sons, Inc., New York, 1960.

17. Greenspan, D.: On the Numerical Solution of Problems Allowing Mixed Boundary Conditions. Journal of the Franklin Institute, January 1964.

18. Williams, M. L.: Stress Singularities Resulting From Various Boundary Conditions in Angular Corners of Plates in Extension. Journal of Applied Mechanics, Vol. 74, 1952.

19. Peaceman, D. W.; and Rachford, H. H., Jr.: The Numerical Solution of Parabolic and Elliptic Differential Equations. Journal Society Indust. Appl. Math., March 1955.

20. Cyrus, N. J.; and Fulton, R. E.: Accuracy Study of Finite Difference Methods. NASA TND-4372, January 1968.

## APPENDIX A

## FINITE DIFFERENCE EQUATIONS

In this section, the partial differential equations of equilibrium are expressed in finite difference format suitable for numerical calculations. The resulting series of difference equations is solved by an iterative procedure which is discussed in Appendix B.

The finite difference expressions for second derivatives are obtained using the "half station" approximation which is the natural result of making the finite difference approximation before expanding the derivatives. This approximation is used because the modulus of elasticity is variable and the results of Reference 20 indicate that the "full station" approximation. Accordingly,

$$\frac{\partial}{\partial z}(Ew_z)_{m,n} = \frac{1}{\Delta z}\left[(Ew_z)_{m,n+1/2} - (Ew_z)_{m,n-1/2}\right]$$

$$= \frac{1}{\Delta z^2}\left[E_{n+1/2}w_{m,n+1} - (E_{n-1/2} + E_{n+1/2})w_{m,n} + E_{n-1/2}w_{m,n-1}\right] \qquad \text{(A-1)}$$

The values of $E$ are evaluated at the temperature of a point midway between grid points $m,n$ and $m,n+1$; $m,n$ and $m,n-1$. Thus equation (A-1) becomes

$$\frac{\partial}{\partial z}(Ew_z) = \frac{1}{\Delta z^2}\left[\frac{(E_n + E_{n+1})}{2}(w_{m,n+1} - w_{m,n}) - \frac{(E_n + E_{n-1})}{2}(w_{m,n} - w_{m,n-1})\right] \quad \text{(A-2)}$$

The finite difference expressions for first derivatives are obtained with the "full station" approximation. Three-point central difference equations are used at interior mesh points and three-point forward differences are used at exterior boundary mesh points.

Interior Points

The equilibrium equations for plane strain are,

$$\frac{\partial}{\partial x}\left[AEu_x + BEw_z + BE\epsilon_y - CE\alpha\,\Delta T\right] + \frac{\partial}{\partial z}\left[DEu_z + DEw_x\right] = 0 \quad \text{(A-3a)}$$

$$\frac{\partial}{\partial z}\left[AEw_z + BEu_x + BE\epsilon_y - CE\alpha\,\Delta T\right] + \frac{\partial}{\partial x}\left[DEu_z + DEw_x\right] = 0 \quad \text{(A-3b)}$$

The values for A,B,C and D are given in Table I.

The finite difference form of these equations is obtained as follows: The first term in equation (A-3a) is obtained by a three-point central difference approximation

$$\frac{\partial}{\partial x}(AEu_x)_{m,n} = \frac{AE_n}{\Delta x^2}\left[u_{m-1,n} - 2u_{m,n} + u_{m+1,n}\right] \quad \text{(A-4)}$$

The second term of equation (A-4), a mixed derivative, is obtained by making a full station approximation in the x-direction before expanding the derivative.

$$\frac{\partial}{\partial x}(BEw_z)_{m,n} = \frac{BE_n}{2\Delta x}\left[w_{z_{m+1,n}} - w_{z_{m-1,n}}\right]$$

$$= \frac{BE_n}{4\Delta x\ \Delta z}\left[w_{m+1,n+1} - w_{m+1,n-1} - w_{m-1,n+1}\right.$$

$$\left. + w_{m-1,n-1}\right] \qquad \text{(A-5)}$$

The third and fourth terms in equation (A-3a) are constant in the x-direction and, therefore, are dropped. The fifth term in equation (A-4) is obtained as shown in equations (A-1) and (A-2).

$$\frac{\partial}{\partial z}(DEu_z)_{m,n} = \frac{D}{\Delta z^2}\left[\frac{(E_n + E_{n+1})}{2}(u_{m,n+1} - u_{m,n}) - \frac{(E_n + E_{n-1})}{2}(u_{m,n} - u_{m,n-1})\right]$$

(A-6)

The sixth term in equation (A4) is obtained in the same manner as equation (A-6) except that E is considered to vary in the z-direction.

$$\frac{\partial}{\partial z}(DEw_x)_{m,n} = \frac{D}{4\Delta x\ \Delta z}\left[E_{n+1}(w_{m+1,n+1} - w_{m-1,n+1}) - E_{n-1}(w_{m+1,n-1} - w_{m-1,n-1})\right]$$

(A-7)

By combining equations (A-4) through (A-7) the finite difference form of equation (A-3a) becomes

$$\frac{AE_n}{\Delta x^2}\left[u_{m-1,n} - 2u_{m,n} + u_{m+1,n}\right] + \frac{BE_n}{4\Delta x\,\Delta z}\left[w_{m+1,n+1} - w_{m-1,n+1}\right.$$

$$\left. - w_{m+1,n-1} + w_{m-1,n-1}\right] + \frac{D}{\Delta z^2}\left[\frac{(E_n + E_{n+1})}{2}(u_{m,n+1} - u_{m,n})\right.$$

$$\left. - \frac{(E_n + E_{n-1})}{2}(u_{m,n} - u_{m,n-1})\right] + \frac{D}{4\Delta x\,\Delta z}\left[E_{n+1}(w_{m+1,n+1} - w_{m-1,n+1})\right.$$

$$\left. - E_{n-1}(w_{m+1,n-1} - w_{m-1,n-1})\right] = 0 \qquad \text{(A-8)}$$

/ similar procedures equation (A-3b) becomes

$$\frac{A}{\Delta z^2}\left[\frac{(E_n + E_{n+1})}{2}(w_{m,n+1} - w_{m,n}) - \frac{(E_n + E_{n-1})}{2}(w_{m,n} - w_{m,n-1})\right]$$

$$+ \frac{B}{4\Delta x\,\Delta z}\left[E_{n+1}(u_{m+1,n+1} - u_{m-1,n+1}) - E_{n-1}(u_{m+1,n-1} - u_{m-1,n-1})\right]$$

$$+ \frac{B\epsilon_y}{2\Delta z}\left[E_{n+1} - E_{n-1}\right] - \frac{C}{2\Delta z}\left[(E\alpha\,\Delta T)_{n+1} - (E\alpha\,\Delta T)_{n-1}\right]$$

$$+ \frac{DE_n}{4\Delta x\,\Delta z}\left[u_{m+1,n+1} - u_{m-1,n+1} - u_{m+1,n-1} + u_{m-1,n-1}\right]$$

$$+ \frac{DE_n}{\Delta x^2}\left[w_{n-1,n} - 2w_{m,n} + w_{m+1,n}\right] = 0 \qquad \text{(A-9)}$$

External Boundary

$$2 \le m \le I - 1, \quad n = J$$

The following procedure is used to obtain the finite difference form of the equilibrium equations at the external boundary. The first term of equation (A-3a) is

$$\frac{\partial}{\partial x}(AEu_x)_{m,n} = \frac{AE_n}{\Delta x^2}\left[u_{m-1,n} - 2u_{m,n} + u_{m+1,n}\right] \qquad \text{(A-10)}$$

The second term in equation (A-3a), $\partial/\partial x\ (BEw_z)$, is obtained using the normal stress boundary condition, that is,

$$\sigma_z = 0 = AEw_z + BEu_x + BE\epsilon_y - CE\alpha\ \Delta T \qquad \text{(A-11)}$$

This gives

$$\frac{\partial}{\partial x}(BEw_z)_{m,n} = -\frac{B^2E_n}{A\ \Delta x^2}\left[u_{m-1,n} - 2u_{m,n} + u_{m+1,n}\right] \qquad \text{(A-12)}$$

The third and fourth terms in (A-3a) are constant in the x-direction and are dropped. The pattern for the fifth term $\partial/\partial z\ (DEu_z)$ is obtained with a three-point "half station" forward difference approximation.

$$\frac{\partial}{\partial z}(DEu_z)_{m,n} = \frac{D}{3\Delta z}\left[8Eu_{z_{m,n}} - 9Eu_{z_{m,n-1/2}} + Eu_{z_{m,n-3/2}}\right] \qquad \text{(A-13)}$$

Applying the shear-stress boundary condition, $(Eu_z)_{m,n} = -(Ew_x)_{m,n}$, equation (A-13) becomes

$$\frac{D}{3\Delta z}\left[-8(Ew_x)_{m,n}\right] + \frac{D}{3\Delta z^2}\left[-\frac{9(E_n + E_{n-1})}{2}(u_{m,n} - u_{m,n-1})\right.$$

$$\left. + \frac{(E_{n-1} + E_{n-2})}{2}(u_{m,n-1} - u_{m,n-2})\right] \qquad \text{(A-14)}$$

The sixth term in (A-3a) is obtained with a three-point "full station" forward difference approximation.

$$\frac{\partial}{\partial z}(DEw_x)_{m,n} = \frac{D}{4\Delta x\ \Delta z}\left[3E_n(w_{m+1,n} - w_{m-1,n})\right.$$

$$\left. - 4E_{n-1}(w_{m+1,n-1} - w_{m-1,n-1}) + E_{n-2}(w_{m+1,n-2} - w_{m-1,n-2})\right] \qquad \text{(A-15)}$$

By combining equations (A-10), (A-12), (A-14), and (A-15) the finite difference form of the equilibrium equation (A-3a) becomes

$$\left(A - \frac{B^2}{A}\right)\frac{E_n}{\Delta x^2}\left[u_{m-1,n} - 2u_{m,n}\ \ u_{m+1,n}\right] + \frac{D}{3\Delta z^2}\left[-\frac{9(E_n + E_{n-1})}{2}(u_{m,n} - u_{m,n-1})\right.$$

$$\left. + \frac{(E_{n-1} + E_{n-2})}{2}(u_{m,n-1} - u_{m,n-2})\right] + \frac{D}{12\Delta x\ \Delta z}\left[-7E_n(w_{m+1,n} - w_{m-1,n})\right.$$

$$\left. - 9E_{n-1}(w_{m+1,n-1} - w_{m-1,n-1}) + 3E_{n-2}(w_{m+1,n-2} - w_{m-1,n-2})\right] = 0 \qquad \text{(A-16)}$$

The finite difference form of the second equilibrium equation (A-3b) is obtained in a similar manner. This equation is

$$\frac{A}{3\Delta z^2}\left[-\frac{9(E_n + E_{n-1})}{2}(w_{m,n} - w_{m,n-1}) + \frac{(E_{n-1} + E_{n-2})}{2}(w_{m,n-1} - w_{m,n-2})\right]$$

$$+ \frac{B}{12\Delta x\ \Delta y}\left[-7E_n(u_{m+1,n} - u_{m-1,n}) - 12E_{n-1}(u_{m+1,n-1} - u_{m-1,n-1})\right.$$

$$\left. + 3E_{n-2}(u_{m+1,n-2} - u_{m-1,n-2})\right] + \frac{B\epsilon_y}{6\Delta z}\left[-7E_n - 12E_{n-1} + 3E_{n-2}\right]$$

$$- \frac{C}{6\Delta z}\left[-7(E\alpha\ \Delta T)_n - 12(E\alpha\ \Delta T)_{n-1} + 3(E\alpha\ \Delta T)_{n-2}\right] = 0 \qquad \text{(A-17)}$$

External Boundary

$$m = I, \quad 2 \leq n \leq J - 1$$

The finite difference form of the equilibrium equations (A-3a) and (A-3b) for this boundary is obtained in the same manner as equations (A-16) and (A-17). The equations are

$$\frac{AE_n}{3\Delta x^2}\left[-9u_{m,n} + 10u_{m-1,n} - u_{m-2,n}\right] + \frac{BE_n}{12\Delta x\ \Delta z}\left[-7(w_{m,n+1} - w_{m,n-1})\right.$$

$$\left. - 12(w_{m-1,n+1} - w_{m-1,n-1}) + 3(w_{m-2,n+1} - w_{m-2,n-1})\right]$$

$$- \frac{8}{3\Delta x}\ BE_n\epsilon_y + \frac{8}{3\Delta x}\ C(E\alpha\ \Delta T)_n = 0 \qquad \text{(A-18)}$$

$$\left(A - \frac{B^2}{A}\right)\frac{1}{\Delta z^2}\left[\frac{(E_n + E_{n+1})}{2}(w_{m,n+1} - w_{m,n}) - \frac{(E_n + E_{n-1})}{2}(w_{m,n} - w_{m,n-1})\right]$$

$$+ \frac{DE_n}{3\Delta x^2}\left[-9w_{m,n} + 10w_{m-1,n} - w_{m-2,n}\right] + \frac{DE_n}{12\Delta x\,\Delta z}\left[-7(u_{m,n+1} - u_{m,n-1})\right.$$

$$\left. - 12(u_{m-1,n+1} - u_{m-1,n-1}) + 3(u_{m-2,n+1} - u_{m-2,n-1})\right] - \frac{C}{2\Delta z}\left(1 - \frac{B}{A}\right)$$

$$\left[(E\alpha\,\Delta T)_{n+1} - (E\alpha\,\Delta T)_{n-1}\right] + \frac{B\epsilon_y}{2\Delta z}\left(1 - \frac{B^2}{A}\right)\left[E_{n+1} - E_{n-1}\right] = 0. \qquad \text{(A-19)}$$

Corner Point

$m = I, \quad n = J$

At this corner point, the normal stresses $\sigma_x$, $\sigma_z$, and the shear stresses are zero. The equilibrium equations are converted to finite difference forms with the following procedure: With E and T constant in the x-direction and with zero shear stress the equilibrium equation (A-3a) becomes

$$\frac{\partial}{\partial x}(AEu_x + BEw_z) = 0 \qquad \text{(A-20)}$$

After substituting the value for $BEw_z$ obtained from the boundary condition $\sigma_z = 0$, equation (A-20) is

$$\frac{\partial}{\partial x}\left[\left(A - \frac{B^2}{A}\right)Eu_x\right] = 0 \qquad \text{(A-21)}$$

Equation (A-21) is expanded with a three-point "half station" difference approximation.

$$\frac{\partial}{\partial x}\left[\left(A - \frac{B^2}{A}\right)Eu_x\right]_{m,n} = \left(A - \frac{B^2}{A}\right)\frac{E_n}{3\Delta x}\left[8(u_x)_{m,n} - 9(u_x)_{m-1/2,n} + (u_x)_{m-3/2,n}\right] \tag{A-22}$$

From the normal stress conditions at the corner point,

$$(u_x)_{m,n} = -\frac{BE_n\epsilon_y + C(E\alpha\,\Delta T)_n}{A + B} \tag{A-23}$$

The finite difference form for equation (A-21) is obtained by combining equations (A-22) and (A-23)

$$\left(A - \frac{B^2}{A}\right)\frac{E_n}{3\Delta x^2}\left[-9u_{m,n} + 10u_{m-1,n} - u_{m-2,n}\right]$$

$$+ \frac{8}{3\Delta x}\left(A - \frac{B^2}{A}\right)\left[-\frac{BE_n\epsilon_y + C(E\alpha\,\Delta T)_n}{A + B}\right] = 0 \tag{A-24}$$

Similarly, the finite difference form of equation (A-3b) is

$$\left(A - \frac{B^2}{A}\right)\frac{1}{3\Delta z^2}\left[-\frac{9(E_n + E_{n-1})}{2}(w_{m,n} - w_{m,n-1}) + \frac{(E_n + E_{n-2})}{2}\right.$$

$$\left.(w_{m,n-1} - w_{m,n-2})\right] - \left(B - \frac{B^2}{A}\right)\frac{\epsilon_y}{2\Delta z}\left[3E_n - 4E_{n-1} + E_{n-2}\right] \cdot$$

$$+ C\left(\frac{B}{A} - 1\right)\frac{1}{2\Delta z}\left[3(E\alpha\ \Delta T)_n - 4(E\alpha\ \Delta T)_{n-1} + (E\alpha\ \Delta T)_{n-2}\right]$$

$$+ \frac{8}{3\Delta z}\left(A - \frac{B^2}{A}\right)\left[-\frac{BE_n\epsilon_y + C(E\alpha\ \Delta T)_n}{A + B}\right] = 0 \qquad \text{(A-25)}$$

Internal Boundary

At the internal boundary the u displacement is zero. Therefore, only the w displacements are unknown and these are obtained from the finite difference form of equation (A-3b) which considering symmetry is

$$\frac{A}{\Delta z^2}\left[\frac{(E_n + E_{n+1})}{2}(w_{m,n+1} - w_{m,n-1}) - \frac{(E_n + E_{n-1})}{2}(w_{m,n} - w_{m,n-1})\right]$$

$$+ \frac{B}{2\Delta x\ \Delta z}\left[E_{n+1}u_{m+1,n+1} - E_{n-1}u_{m+1,n-1}\right] + \frac{B\epsilon_y}{2\Delta z}\left[E_{n+1} - E_{n-1}\right]$$

$$- \frac{C}{2\Delta z}\left[(E\alpha\ \Delta T)_{n+1} - (E\alpha\ \Delta T)_{n-1}\right] + \frac{DE_n}{2\Delta x\ \Delta z}\left[u_{m+1,n+1} - u_{m+1,n-1}\right]$$

$$+ \frac{DE_n}{\Delta x^2}\left[-2w_{m,n} + 2w_{m+1,n}\right] = 0 \qquad \text{(A-26)}$$

Internal Corner

The finite difference form of equation (A-3b) for this corner point is obtained in the same manner as equation (A-17) and is

$$\frac{A}{3\Delta z^2}\left[-\frac{9(E_n + E_{n-1})}{2}(w_{m,n} - w_{m,n-1}) + \frac{(E_{n-1} + E_{n-2})}{2}(w_{m,n-1} - w_{m,n-2})\right]$$

$$+ \frac{B}{6\Delta x\,\Delta z}\left[-7E_n u_{m+1,n} - 12E_{n-1}u_{m+1,n-1} + 3E_{n-2}u_{m+1,n-2}\right] + \frac{BK}{6\Delta z}\left[-7E_n\right.$$

$$\left. - 12E_{n-1} + 3E_{n-3}\right] - \frac{C}{6\Delta z}\left[-7(E\alpha\,\Delta T)_n - 12(E\alpha\,\Delta T)_{n-1}\right.$$

$$\left. + 3(E\alpha\,\Delta T)_{n-2}\right] = 0 \qquad \text{(A-27)}$$

The finite difference equations given in this Appendix are solved for u and w displacements with a digital computer program which was written as part of this investigation. Some details of this computer program are given in Appendix B.

TABLE I.- VALUES OF CONSTANTS IN THE EQUILIBRIUM AND STRESS EQUATIONS

| | Plane strain | Plane stress |
|---|---|---|
| A | $\frac{1 - \nu}{(1 + \nu)(1 - 2\nu)}$ | $\frac{1}{(1 - \nu^2)}$ |
| B | $\frac{\nu}{(1 + \nu)(1 - 2\nu)}$ | $\frac{\nu}{(1 - \nu^2)}$ |
| C | $\frac{1}{(1 - 2\nu)}$ | $\frac{1}{(1 - \nu)}$ |
| D | $\frac{1}{2(1 + \nu)}$ | $\frac{1}{2(1 + \nu)}$ |

## APPENDIX B

This section describes the procedure used to solve the finite difference equations of Appendix A for the u and w displacements of each mesh point. The method for calculating stresses from these displacements is also discussed.

Since the present analysis is concerned with edge stresses, it is necessary to use relatively small mesh spacing which in turn requires the solution of large sets of simultaneous equations. These equations are solved by an alternating direction method (see Ref. 19) programed for a Control Data Corp. 6600 Digital Computer. The alternating direction procedure is based on a line-by-line solution of relatively small sets of simultaneous equations that can be solved by direct, noniterative methods. With this method the finite difference formulations for equation (A-3a) are solved for u displacements and similarly the w displacements are obtained from the finite difference formulations of equation (A-3b).

The displacement calculations are started by assuming values for the u and w displacements at each mesh point. The u and w displacements at mesh points in each horizontal line are calculated and stored. The displacements in each vertical line are then calculated and compared to the stored values. The calculations of displacements are continued line-by-line until the absolute values from successive iterations agree within a specified percentage. The coefficient matrices for $u_{m,n}$ and $w_{m,n}$ are tridiagonal in both the horizontal

and vertical directions except on the boundaries $x = b$ and $z = h$. At these boundaries the coefficients are modified by an algebraic transformation so that each set of simultaneous equations can be solved by a direct factoring method.

The number of iterations required to achieve a selected convergence varies with the number of mesh points. A convergence accelerating factor is not used, but a procedure is programed whereby the displacements calculated for a coarse mesh spacing are used as initial inputs for successively finer mesh spacings. This procedure produces significant savings in computer time. No problems of stability are encountered since the program solves steady-state elliptic equations.

The normal and shear stresses at each mesh point are calculated with the finite difference forms of the following equations:

$$\sigma_x = AEu_x + BEw_z + BE\epsilon_y - CE\alpha\,\Delta T \tag{B-1}$$

$$\sigma_z = AEw_z + BEu_x + BE\epsilon_y - CE\alpha\,\Delta T \tag{B-2}$$

$$\tau_{xz} = D(Eu_z + Ew_x) \tag{B-3}$$

Equations (B-1), (B-2), and (B-3) are programed using three-point central differences for interior mesh points and three-point forward differences for external boundary mesh points. The computer program

uses the displacements computed for each mesh point to evaluate the strain values in equations (B-1), (B-2), and (B-3) with the exception of $\epsilon_y$ which is constant for this analysis.